

Predicting overpressure using basin modeling software

Jens-Erik Lund Sneek

Abstract—It is notoriously difficult to predict porosity and pore pressure in buried sedimentary rocks, particularly if they have experienced a complex geologic history. Many techniques exist to estimate overpressure using geophysical imaging methods, but basin and petroleum systems modeling (BPSM) software also holds great potential for making independent estimates of pore pressure, effective stress, and porosity, due to its ability to model the 3D geologic history of a sedimentary basin.

In this term paper, I first discuss the modeling capabilities of industry standard PetroMod BPSM software. I then attempt to replicate results of an isotropic rock compression experiment using a basic 1D BPSM model. This test highlights PetroMod’s impressive ability to incorporate customized compaction criteria, but it also shows that the lack of ability to model elastic rebound of porosity introduces significant limitations for modeling porosity and pore pressure. I then conduct 3D tests in PetroMod in order to determine whether BPSM might reveal hard overpressure in sediments having otherwise normal porosity values that might hence go undetected using traditional geophysical overpressure detection methods. These analyses show that BPSM indeed presents great unique ability to predict overpressure. These capabilities will become significantly more accurate as future software releases incorporate the capability to model additional geologic processes.

I. INTRODUCTION

DESPITE decades of study, it remains difficult to predict porosity, pore pressure, and permeability of strata buried in sedimentary basins (e.g. Dutta, 2002; Sayers et al., 2002; Zimmer et al., 2002; Zimmer, 2004; Chopra and Huffman, 2006; Gutierrez et al., 2006; Zimmer et al., 2007a, b; Zhang, 2011; Burgreen-Chan et al., 2015). Accurate prediction of these parameters would be of substantial assistance for numerous applications, most notably for predicting drilling hazards, better understanding hydrocarbon migration histories, and constraining maximum column heights in petroleum prospects.

One especially difficult problem is meaningfully predicting porosity gain and pore pressure change as rocks

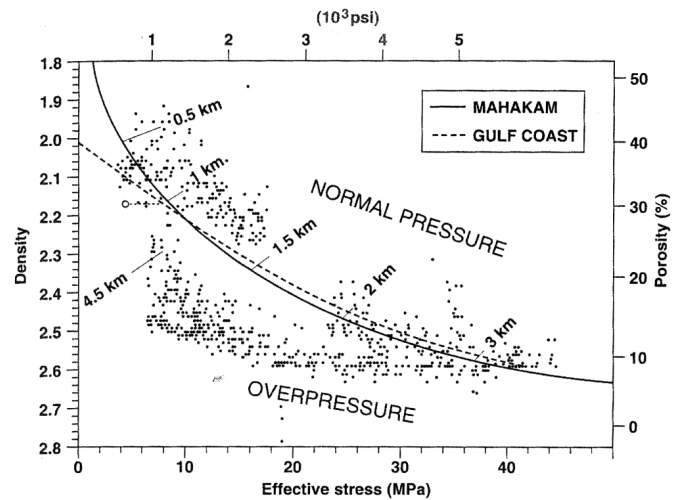


Fig. 1: Figure 2.18b from Zoback (2010) showing a typical burial trend for porous sedimentary rocks having hydrostatic pore pressures (“normal pressure”). Effective stress increases as the rocks are buried, resulting in asymptotic porosity loss as measured by the increasing measured density values. These rocks subsequently experience a loss of effective stress during the onset of overpressure. The loose trend of data labeled “overpressure” shows that a small degree of porosity gain occurs as effective stress decreases.

become overpressured. The inability to adequately constrain these values could result in serious hazards to drilling operations because unanticipated pockets of hard overpressure can cause catastrophic well blowouts. Figure 1 illustrates this problem by demonstrating the wide range of effective stresses (and hence pore pressures) that could be associated with a given porosity value in overpressured sedimentary rocks.

Numerous methods exist that attempt to predict porosity and pore pressure using seismic reflection surveys, but some of these methods are limited by their expectation that porosity should increase as overpressure increases (see Dutta, 2002; Chopra and Huffman, 2006; Gutierrez et al., 2006; Zhang, 2011, for discussion). This might be a problematic assumption in sediments that have already undergone significant compaction due to

nonrecoverable loss of porosity that occurs during burial (Figure 1). Therefore, understanding sediment burial, thermal history, petroleum generation and migration, and stress evolution using basin modeling software has potential to provide additional predictive power. But while basin and petroleum system modeling (BPSM) software and interpretive techniques have made dramatic advances in recent years (e.g. Al-Hajeri and Al Saeed, 2009; Hantschel and Kauerauf, 2009; Peters et al., submitted), even the most sophisticated programs remain limited by the quality of a user's *a priori* knowledge of basin geology, as well as the program's ability to accurately model the full range of physical processes that occur during sediment burial and unloading, and the applicability of selected rock physics parameters.

In this term paper I conduct four simple tests to investigate the poroelastic modeling capabilities of PetroMod. In the first, I consider simple loading and unloading trends for a 1D model and I compare my results against published rock physics experimental values. In the last three tests, I construct a basic 3D model and evaluate the pore pressure, porosity, and stress histories resulting from compaction and petroleum maturation.

To lay the groundwork for these simple experiments, I begin by outlining the theoretical and empirical background for overpressure and poroelasticity. I also discuss the modeling capabilities of Schlumberger's industry standard PetroMod software. I then provide methodological details and results from this study. I conclude by discussing implications of my work for pore pressure prediction and BPSM software.

II. BACKGROUND

A. Development of overpressure

When sediment is first deposited, fluid occupying pore space is assumed to be in pressure communication with surface waters through tortuous pore pathways. Under these conditions, fluid pressure will be hydrostatic throughout the connected column (Figure 2). As sediment is buried, vertical stress accumulates rapidly, compressing the rock and resulting in dewatering as porosity decreases (Swarbrick et al., 2002). As this proceeds, permeability decreases, pore space may

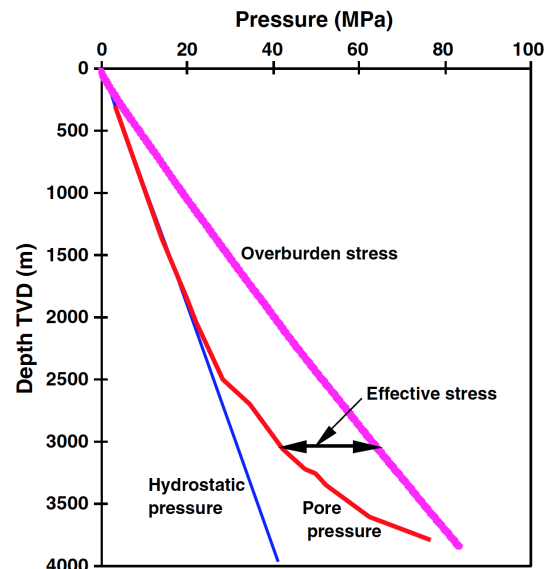


Fig. 2: Cartoon illustration from Zhang (2011) showing the definitions of overpressure (deviation from hydrostatic) and Terzaghi (simple) vertical effective stress ($\sigma_v = S_v - P_f$).

become isolated, and fluids will hence no longer be connected to pathways leading to the surface. A rate of compaction in excess of the rate that would allow fluid communication to the surface is called *disequilibrium compaction*. When this occurs, fluid pressures below or above hydrostatic may develop (underpressure and overpressure, respectively; Figure 2). Overpressure is common in sedimentary basins.

The shallowest depth at which overpressure develops in a vertical section is called the fluid retention depth (FRD), and this depth is mostly controlled by the rate of sedimentation (Swarbrick et al., 2002). Higher sedimentation rates are typically associated with shallower FRDs (Figure 4). Below the FRD, P_p gradient is often parallel to the lithostatic gradient, rather than the hydrostatic gradient, and this is consistent with a lack of pressure communication to the surface (Swarbrick et al., 2002).

Disequilibrium compaction, described above, is the factor that contributes most to overpressure (Swarbrick et al., 2002), as shown in Figure 5. In addition to the main contribution from accumulating vertical stress, overpressure can be aided by horizontal tectonic compression, which can further reduce pore space and limit permeability (Swarbrick et al., 2002).

Fluid expansion also contributes to overpressure (Figure 5) but this is typically a small factor except for in the

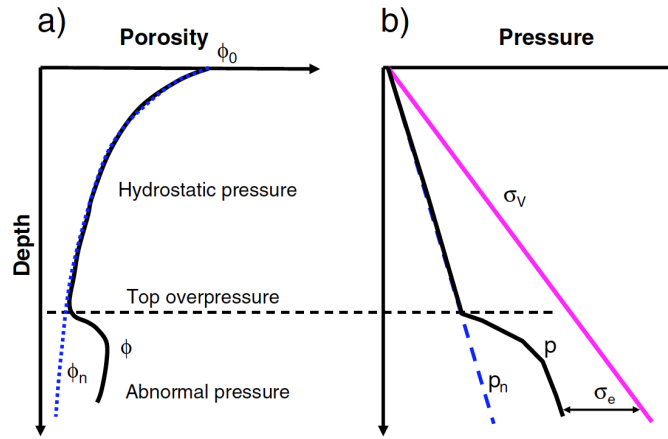


Fig. 3: Schematic illustrations of porosity and pressure versus depth from Zhang (2011). “Top overpressure” is the same as the onset of fluid retention. ϕ is porosity (%) and ϕ_0 refers to the initial porosity shortly after deposition. ϕ_n indicates a normal compaction trend. σ_v is vertical or overburden stress, p is actual pore fluid pressure, p_n is a normal pore fluid pressure trend during burial, and σ_e is vertical effective stress (referred to as σ_v in this term paper). Pore fluid pressure is referred to as P_p in the remainder of this term paper.

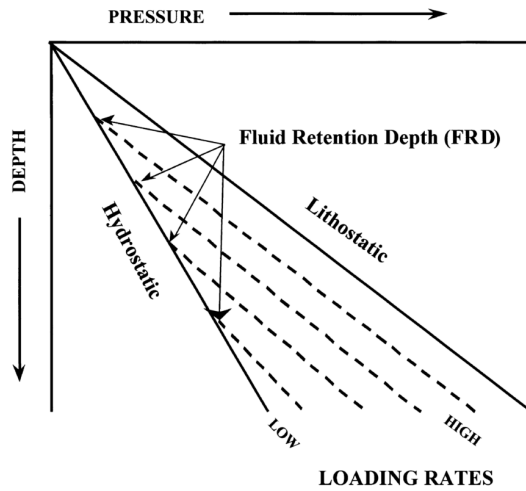


Fig. 4: Schematic figure from Swarbrick et al. (2002) showing the effect of different sedimentary loading rates on fluid retention depth and degree of overpressure attained at a given depth. At higher loading rates, fluid retention depth (and onset of overpressure) typically occurs at shallower depths, resulting in greater degrees of overpressure at a given depth.

case of cracking to petroleum gas, which is associated with large volume increases (Swarbrick et al., 2002). In addition, buoyant hydrocarbons can significantly increase overpressure if they migrate into a reservoir. Other processes, such as thermal expansion of water or volume changes associated with the smectite to illite transition during diagenesis (Figure 5) contribute in a minor way to overpressure magnitudes (Swarbrick et al., 2002).

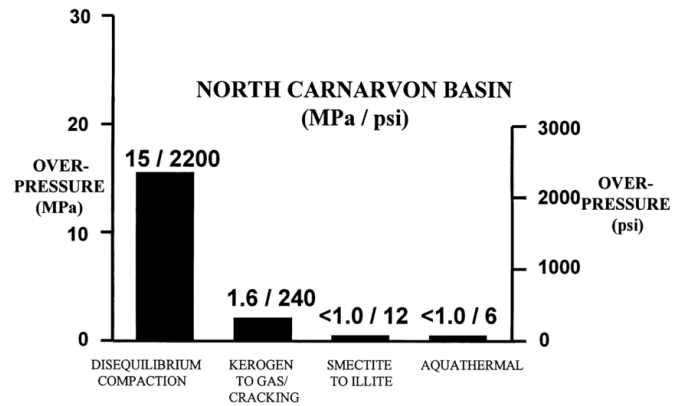


Fig. 5: Chart from Swarbrick et al. (2002) and references therein showing the relative contribution various processes to overpressure generation in the North Carnarvon Basin, Australia.

B. Pore pressure and poroelasticity

The stresses, S , acting on any point within a body can be defined by the tensor

$$S_{ij} = \begin{bmatrix} S_{11} & S_{12} & S_{13} \\ S_{21} & S_{22} & S_{23} \\ S_{31} & S_{32} & S_{33} \end{bmatrix} = \begin{bmatrix} S_{11} & S_{12} & S_{13} \\ S_{12} & S_{22} & S_{23} \\ S_{13} & S_{23} & S_{33} \end{bmatrix}.$$

Three mutually perpendicular principal stress orientations are typically defined in the earth, each of which represents an axis of normal stress (no shear component) acting on a point in the subsurface, as expressed by

$$S = \begin{bmatrix} S_1 & 0 & 0 \\ 0 & S_2 & 0 \\ 0 & 0 & S_3 \end{bmatrix},$$

where S_1 is the maximum principal stress, S_2 is intermediate, S_3 is the least principal stress, and $S_{00} = \frac{1}{3}(S_1 + S_2 + S_3)$ (Zoback, 2010). Because no shear can be resolved onto an interface between solid matter and a fluid such as air, the principal stresses are typically oriented based on their relationship to the earth's surface, which is assumed to be horizontal. This is a reasonable assumption when we consider stresses acting far below the earth's surface, where stress perturbations due to gravity should be extremely small. Thus, one principal stress is vertical (S_V) and the other two are horizontal ($S_{H_{max}}$ and $S_{h_{min}}$). The magnitude of S_V at any point in the subsurface is typically equal to the weight of overlying material, whereas $S_{H_{max}}$ and $S_{h_{min}}$ are controlled in part by tectonic processes such as the ridge push force.

Strain, ϵ , results from applied stresses, and can be described using a similar tensor to the stress tensor:

$$\epsilon_{ij} = \begin{bmatrix} \epsilon_{11} & \epsilon_{12} & \epsilon_{13} \\ \epsilon_{21} & \epsilon_{22} & \epsilon_{23} \\ \epsilon_{31} & \epsilon_{32} & \epsilon_{33} \end{bmatrix} = \begin{bmatrix} \epsilon_{11} & \epsilon_{12} & \epsilon_{13} \\ \epsilon_{12} & \epsilon_{22} & \epsilon_{23} \\ \epsilon_{13} & \epsilon_{23} & \epsilon_{33} \end{bmatrix}.$$

When oriented such that a point experiences no shear strain, this tensor likewise simplifies to

$$\epsilon = \begin{bmatrix} \epsilon_1 & 0 & 0 \\ 0 & \epsilon_2 & 0 \\ 0 & 0 & \epsilon_3 \end{bmatrix},$$

where $\epsilon_{00} = \epsilon_1 + \epsilon_2 + \epsilon_3$ (Zoback, 2010). It is possible to relate axial strain, ϵ_{11} , to lateral strain, ϵ_{33} , through Poisson's ratio: $\nu = -\frac{\epsilon_{33}}{\epsilon_{11}}$. ϵ in turn can be related to S through numerous relationships. For example, Young's Modulus relates axial stress to axial strain: $E = \frac{S_{11}}{\epsilon_{11}}$.

As defined thus far, the magnitudes of S are independent of the pressure of fluids occupying pore space (P_p). Because P_p acts against the remotely applied stresses, its effect in an elastic medium is accounted for by the effective stress variable σ (Figure 2), defined using the simple Terzaghi relationship $\sigma_{ij} = S - \delta_{ij}P_p$ (von Terzaghi, 1923; Nur and Byerlee, 1971; Zoback, 2010). The Kronecker delta, δ_{ij} , ensures that P_p is mapped only onto the diagonals of the second order σ_{ij} tensor because it is defined as $\delta_{ij} = 1$ if $i = j$, else $\delta_{ij} = 0$ if $i \neq j$.

Unfortunately, this simple relationship assumes that

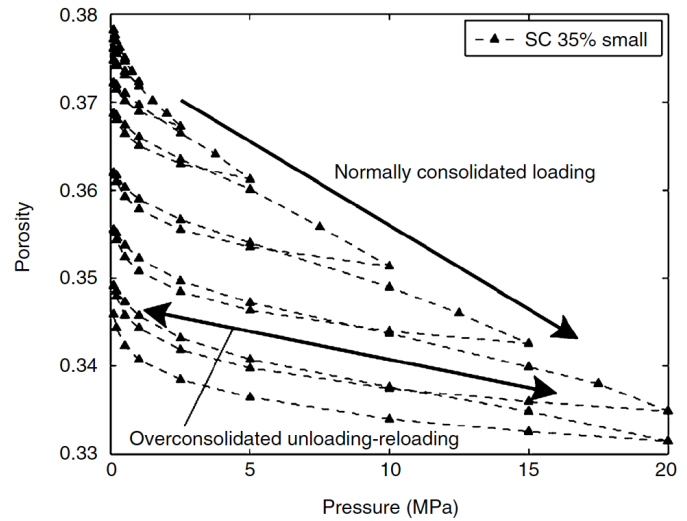


Fig. 6: Figure from Zimmer et al. (2007b) showing laboratory results for porosity changes during repeated loading (paths with increasing pressure and decreasing porosity) and unloading (paths showing decreasing pressure and slightly decreasing porosity) of a “typical sand” sample “SC 35% small.”

P_p is equally effective in all rock types to counteract the remotely applied stresses (S). In reality, the compressibility of different rock types varies widely, in part because of varying ϕ (e.g. Nur and Byerlee, 1971). This is described by the “Biot coefficient,” α , where $\alpha = 1 - \frac{K_b}{K_g}$, $0 \leq \alpha \leq 1$, and where K_b and K_g are the bulk moduli (stiffness) of the drained rock and its solid grains, respectively (Biot, 1941; Nur and Byerlee, 1971; Zoback, 2010). The bulk modulus, K , is defined as $K = \frac{S_{00}}{E_{00}}$ and is the inverse of compressibility. Therefore, $\alpha = 0$ represents a material whose compressibility is completely independent of pore pressure (and therefore may lack porosity). In contrast, when $\alpha = 1$ the compressibility of the porous material is entirely controlled by P_p . In light of this relationship, the effective stress equation can be rewritten as $\sigma_{ij} = S - \delta_{ij}\alpha P_p$ (Nur and Byerlee, 1971; Zoback, 2010, and references therein).

During burial, the vertical stress (S_V) increases, and so too do the horizontal stresses ($S_{H_{max}}$ and $S_{h_{min}}$). As this occurs, ϕ decreases in an asymptotic fashion (Figure 1) that is lithology-specific and caused by a combination of elastic (recoverable) and plastic (non-recoverable) processes (Bowers, 2002; Hantschel and Kauerauf, 2009; Zoback, 2010). This can be modeled with formulae such as Athy's Law, $\phi = \phi_0 e^{-u\sigma_v}$, where

ϕ_0 is the initial porosity and u is a compaction constant (Athy, 1930; Hantschel and Kauerauf, 2009).

Two primary processes can reduce the stress acting on the pore space and hence partially reverse this process: an increase in P_p , which reduces σ , or exhumation, which directly reduces S_V . However, as shown in Figure 1, the majority of porosity loss is typically a result of nonrecoverable pore destruction, and only a small component of elastic rebound occurs.

A practical consideration is that this phenomenon can lead to pore pressures that are far in excess of what would be expected from simple analysis using a theoretical compaction curve that relates P_p to porosity or formation depth (Bowers, 2002; Zoback, 2010). The risk posed by this phenomenon can be observed by comparing Figures 1, 3, and 6; although Figure 3 illustrates the expectation that ϕ should increase as overpressure develops, Figures 1 and 6 show that the decrease in σ that occurs during overpressure development only results in a small increase in ϕ . Thus, geophysical techniques might not identify areas of overpressure if the positive porosity anomaly in a sedimentary unit is not sufficiently large due to nonrecoverable porosity loss during normal compaction.

Laboratory studies such as those by Zimmer et al. (2007b) also find a similar loading and unloading pattern (Figure 6). In his study, Zimmer et al. (2007b) examined the change of ϕ and other parameters for sand samples during isotropic compression. For a reconstituted sample composed of 35% by mass of 0.053–0.088 mm size grains and 65% of 0.295–0.350 mm size grains that was saturated in water, that study found that ϕ decreases in an asymptotic manner during isotropic compression. However, small degrees of elastic porosity recovery occurred during periodic unloading events.

Finally, it is also known that, through faulting, pore pressure modulates stresses, and faulting in turn modulates pore pressures (Sibson and Scott, 1998; Townend and Zoback, 2000; Finkbeiner et al., 2001; Zoback and Townend, 2001; Sibson, 2003; Sutherland et al., 2012; Lund Snee et al., 2014; Burgreen-Chan et al., 2015). Pore pressure exerts first-order control on the likelihood of faults to slip. Elevated pore pressures from

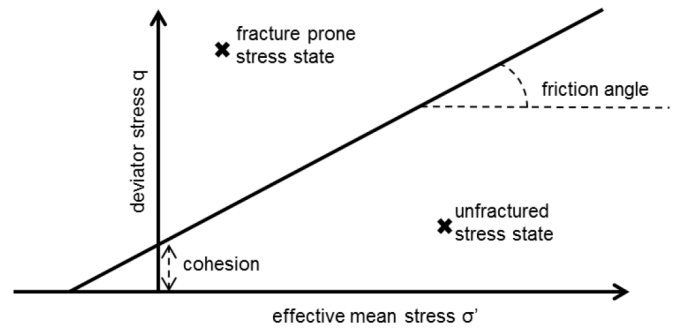


Fig. 7: Cartoon plot from Schlumberger (2014b) showing the type of rock failure criterion applied by PetroMod v.2014-1.

overpressured sedimentary rocks that infiltrate existing faults will increase the likelihood of slip according to

$$\tau = \mu_s \sigma_n = \mu_s (S - P_p), \quad (1)$$

where μ_s is the coefficient of sliding friction (Sibson and Scott, 1998; Sibson, 2003). Values of τ in excess of this envelope for a given σ will result in brittle shear failure (see Figure 7). A typical value for μ_s in sedimentary rocks is 0.6 (Byerlee, 1978; Zoback, 2010), and it is reasonable to expect that this value would be higher for inducing shear in unfaulted rocks (Sibson, 2003).

Faulting releases P_p and increases bulk crustal permeability by creating transient fluid pathways (Townend and Zoback, 2000; Zoback and Townend, 2001). This has implications also at a reservoir scale because the low density of hydrocarbons relative to brine facilitates development of overpressure in petroleum reservoirs, and overpressure can result in hydrocarbon escape.

Because this relationship between elevated P_p and faulting along relatively weak existing faults modulates P_p at crustal and finer scales, it results in a stronger crust than would be expected if P_p could build to near-lithostatic values (Zoback and Townend, 2001). Thus, compared with the likelihood of fault slip, it is rare for elevated pore pressures to induce tensile fracturing. Initial tensile fracture formation requires extremely high P_p that has not escaped through other means, as well as a condition in which $S_1 - S_3 < 4T$, where T is the tensile strength of the rock (e.g. Sibson and Scott, 1998; Finkbeiner et al., 2001; Sibson, 2003).

A study of sedimentary rocks in the East Coast Basin of New Zealand emphasizes the extent to which stress

conditions play an important role for controlling faulting, P_p , and hydrocarbon column heights (Burgreen-Chan et al., 2015). Using BPSM, the authors found that P_p likely increased as a result of tectonic shortening, which increased horizontal stresses on the basin sediments. In addition, the elevated pore pressures modulated differential stresses such that small perturbations in far-field stresses could change the stress regime within parts of the basin. This is in agreement with observations that stresses tend to become more isotropic at higher magnitudes of overpressure because, as we have seen, P_p decreases frictional strength of faults, leading to relaxation of differential stresses (Zoback, 2010).

C. Capabilities of PetroMod v.2014-1 software

PetroMod v.2014-1 is industry standard BPSM software that has sophisticated capabilities to model porosity, permeability, fluid migration, compaction, stresses, thermal characteristics, hydrocarbon maturation, and other factors in 1D, 2D, or 3D over time. The software allows user control over factors such as the relationship between ϕ and permeability, k , including the option to require a unit to act as a perfect seal (completely impermeable), apply the Kozeny-Carman model (Carman, 1956), or apply a user-defined formula (Schlumberger, 2014b). It is also possible to prescribe relative permeabilities for fluid phases in different lithologies within the model.

PetroMod's Lithology Editor module enables the user to prescribe fluid seal properties of a lithology. A user may select various options that relate capillary entry pressure to seal permeability or porosity, or may provide a custom formula for capillary entry pressure, including the ability of a unit to act as a "perfect seal" (Schlumberger, 2014b). It is also possible to use the software to calculate the maximum column height that may be held below a seal of a certain porosity, or alternatively to calculate the porosity and capillary entry pressure needed to hold a given fluid column (Schlumberger, 2014b). In addition, a user may select a pore pressure above which a lithology fractures. If fracturing occurs, PetroMod decreases capillary entry pressure and increases permeability in that unit (Schlumberger, 2014b).

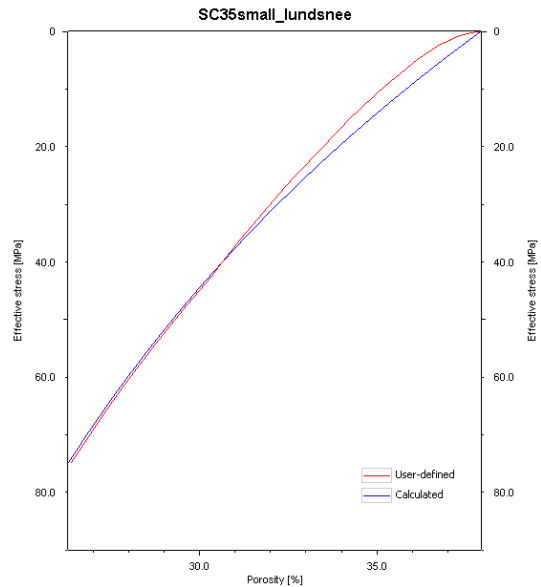


Fig. 8: Compaction curve employed in Experiment 1 (red curve). This custom curve was based on the porosity values obtained during a laboratory isotropic compression and unloading experiment (Figure 6) for the synthetic sand sample "SC 35% small" (Zimmer, 2004; Zimmer et al., 2007b). ϕ was lower for a given effective stress during subsequent cycles as a result of nonrecoverable porosity loss during initial compaction up to that stress magnitude. Therefore, I only employed values for the first time a particular σ magnitude was reached during the laboratory experiments. I manually fit values for $\sigma > 20$ MPa to an Athy-type compaction curve (blue curve) with grain density $\rho_g = 2605.5 \text{ kg m}^{-3}$, $\phi_0 = 37.94\%$, $\phi_{min} = 16\%$, and Athy's factor $A = 10.11 \text{ GPa}^{-1}$ (Appendix C). Values for ϕ_0 and ρ_g were based on values reported by Zimmer (2004).

Besides considering P_p when determining the likelihood of fracturing, PetroMod can apply a failure criterion with variable cohesion and friction values (Figure 7). This criterion provides a threshold ratio of deviator stress ($q = [(\sigma_1 - \sigma_2)^2 + (\sigma_1 - \sigma_3)^2 - (\sigma_2 - \sigma_3)^2]^{\frac{1}{2}}$) to effective mean stress ($\sigma_{00} = \frac{1}{3}(\sigma_1 + \sigma_2 + \sigma_3)$) above which fracturing is considered likely (Schlumberger, 2014b).

A number of 3D stress and rock strength modeling capabilities are currently built into PetroMod, including the option to apply relationships between σ and ϵ that consider poroelasticity. Poroelasticity may also be disabled. PetroMod's poroelastic capabilities relate σ , ϵ , and a stiffness tensor C though $\sigma_{ij} = C_{ijkl}\epsilon_{kl} + \alpha P_p \delta_{ij}$, where α can be set for any lithology and C is itself a function of E and ν (Schlumberger, 2014b). To my knowledge, PetroMod does not yet consider thermo-poroelasticity (Zoback, 2010; Schlumberger, 2014b).

PetroMod provides the option for ν or E (or both) to change with evolving ϕ during simulation. If any of

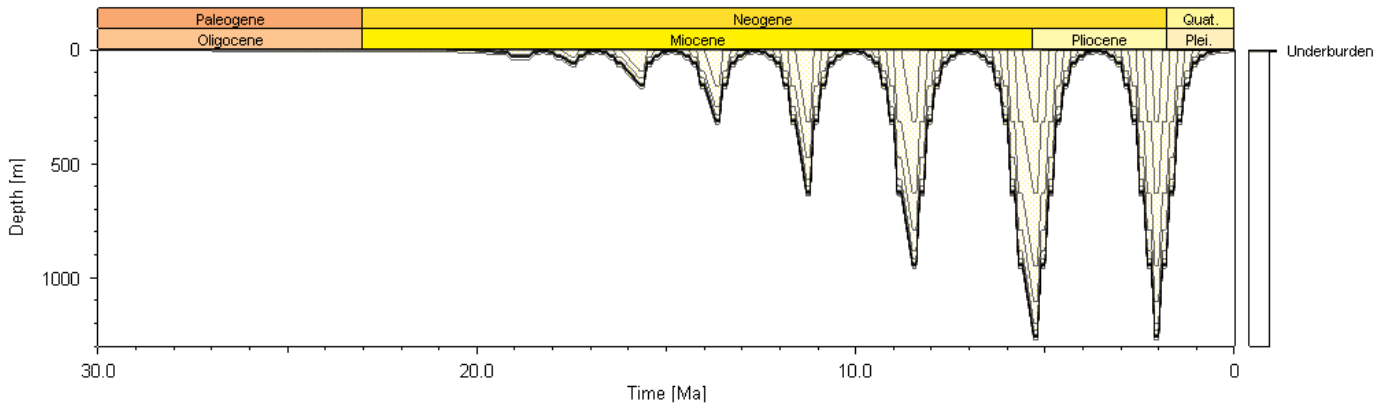


Fig. 9: Burial history curve for Experiment 1. The thickest (and most clearly visible) units in each depositional cycle represent overburden. These peaks are underlain by a thin “reservoir” test unit (1 m thick in order to reduce compaction of this unit under its own weight) and a 10 m basal “underburden” unit. The reservoir unit is too thin to observe in this figure but the thin underburden is visible at the bottom of the succession. At the end of the model run, only underburden and reservoir strata remain uneroded. Thicknesses of overburden units correspond to sequential additions of stress applied during the experiment reported by Zimmer (2004). See Appendix A for the raw data reported by Zimmer (2004). Appendix B shows my calculations for the corresponding thicknesses of sediment deposited or eroded at $\rho_{\text{overburden}} = 1617 \text{ kg m}^{-3}$. The custom overburden lithology was set as noncompressible, and I disabled radiogenic heat production in order to prevent thermally influenced compaction or diagenetic behavior.

these options are enabled, the program interpolates in a linear fashion between initial and minimum values of ϕ . Alternatively, E may be calculated from the compressibility determined from the basic Terzaghi effective stress relationship, C_T , at a given time step during compaction using $E(\phi) = \frac{(1-2\nu)(1+\nu)}{(1-\nu)C_T(\phi)}$ (Schlumberger, 2014b). PetroMod also has the capability to consider anisotropy of poroelasticity values with respect to bedding orientation.

During simulation of a 2D or 3D model, PetroMod is able to account for the evolution of rock stress. It is possible to overlay rock stress values over time on a simulated model, and the modeled stress values can be set to account for poroelastic parameters set for each lithology or, alternatively, for poroelastic moduli calculated from the entire compaction curve (Schlumberger, 2014a). In addition, PetroMod provides capabilities for calculating pressures based on stress values, a capability that is of interest for those seeking to employ BPSM techniques to predict overpressure. Together, these capabilities provide numerous opportunities for testing porosity, pore pressure, and stress evolution in a sedimentary basin setting.

III. METHODS

A. Experiment 1: Effect of loading and unloading in 1D

To develop experimental burial histories, test BPSM software capabilities, and evaluate various lithological,

fluid, and stress parameters, I created a simple 1D basin model using Schlumberger’s PetroMod v.2013-2 (this is one release older than the version described above, but the capabilities are similar). The stratigraphy consists of a 10 m custom “underburden” that is an impermeable, uncompactible shale producing no radiogenic heat (Figure 9). The overlying 1 m thick “reservoir” sand is intended to match the lithological parameters for sample “SC 35% small” tested by Zimmer (2004) and Zimmer et al. (2007b). A custom compaction curve was created for this lithology (see Appendix C) to match the compaction history observed during their laboratory experiment, and an Athy-type curve was fit for σ values greater than 20 MPa (Figure 8). A 1D model is appropriate for replicating these laboratory results, especially because in 1D PetroMod assumes isotropic stresses that are equal to the overburden stress. Two simulation cycles were conducted by PetroMod for each test.

Using this simple model, I first tested the software’s predictions of effective stress, pore pressure, and porosity using a cycling burial history (shown in Figure 9) approximately matching the experimental loading and unloading stress paths employed by Zimmer et al. (2007b), as shown in Figure 6. To match Zimmer et al. (2007b)’s analytical conditions, my model employed isotropic stresses. I employed ca. 0.1 Ma time steps

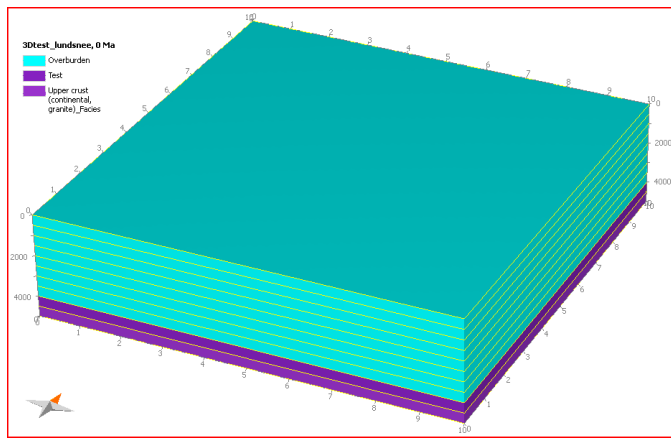


Fig. 10: Basic 3D model employed for Experiments 2–4. The tested “reservoir” unit is shown in dark purple, and it is underlain by a crystalline underburden lithology (medium purple). These units are overlain by 8 shale units (teal). Model measures 10 km wide × 10 km deep × 5 km thick. All units were initially 500 m thick.

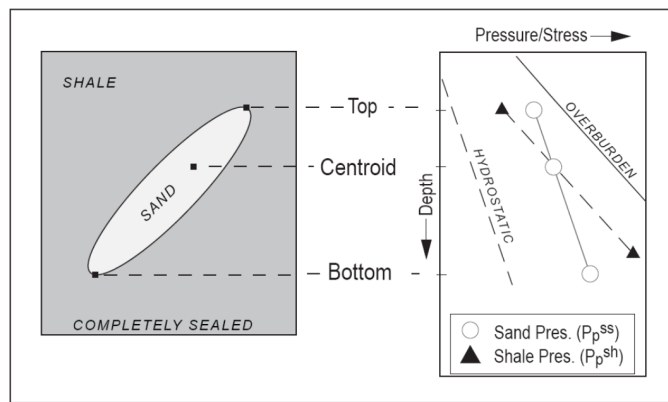


Fig. 11: Schematic figure from Zoback (2010) showing relative stress or pressure conditions resulting from the centroid effect.

between each data point of Zimmer et al. (2007b) and ensured that strata thicknesses deposited or eroded at each step resulted in overburden stresses corresponding exactly to each step in the laboratory tests.

B. Experiment 2: Effect of compaction in 3D

For Experiment 2, I created a simple 3D model (Figure 10). “Layercake” stratigraphy (flat-lying and lacking any structure) was employed in order to avoid complications to pore pressure such as the “centroid effect.” The centroid effect refers to a phenomenon that develops when a dipping sandstone or other permeable unit is encased in low-permeability strata (Figure 11). Because hydrostatic fluid pressure gradients are “steeper” than most lithostatic gradients (meaning that fluid pressures increase much less rapidly with depth than do overbur-

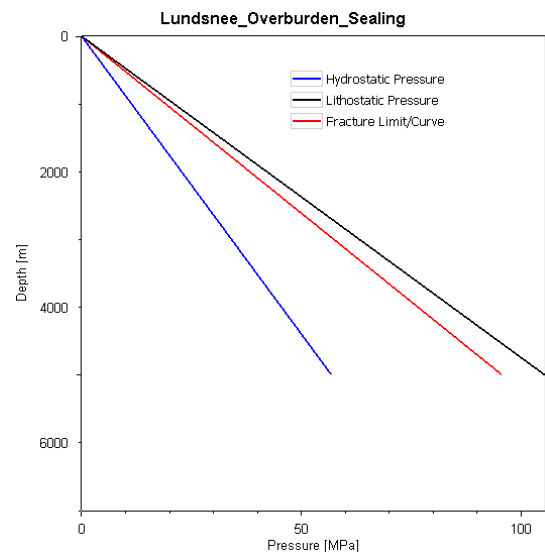


Fig. 12: Example fracture gradient employed for all lithologies except for the basement in the 3D modeling experiments. Fracture gradient is set to a default 80% of the difference between hydrostatic and lithostatic. Fracturing occurs when stresses exceed this threshold.

den pressures), the shallowest portion of the dipping, permeable unit will attain pore pressures in excess of those in the encasing strata (Figure 11). In contrast, the deepest portion of the high-permeability unit will have anomalously low pore pressures for that depth.

This model measures 10 km wide × 10 km deep × 5 km thick and includes used 10 stratigraphic units of equal (500 m) thickness (Figure 10). The lowest unit is composed of impermeable crystalline “basement” (the default “Upper crust (continental, granite)”) that is set to be uncompactible. This is overlain by the “reservoir” unit of interest, which is the default “Shale (typical)” incorporated into the PetroMod software. The reservoir is in turn overlain by 8 layers composed of the same “Shale (typical)” lithology. Default compaction curves for “Shale (typical)” were applied to both the reservoir and overburden (Figure 13).

Each unit was deposited continuously over 10 Ma, and no hiatus occurred before deposition of the next unit. Thermal conductivities, heat capacities, and radiogenic heat production were not changed from default values. Fracture limit was set to a default of 80% of the difference between hydrostatic and lithostatic (Figure 12).

This experiment consisted of a “base case” run, in which the overburden and underburden had default com-

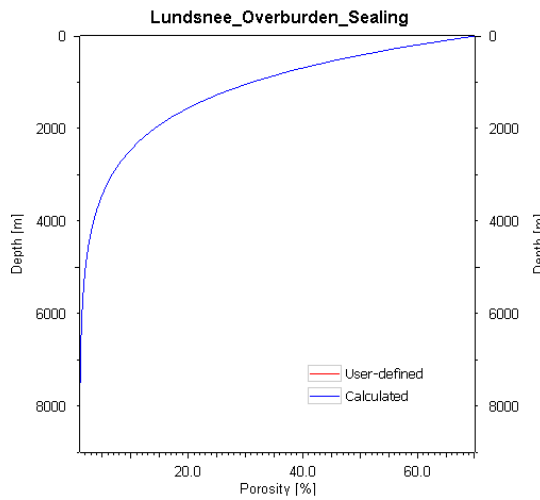
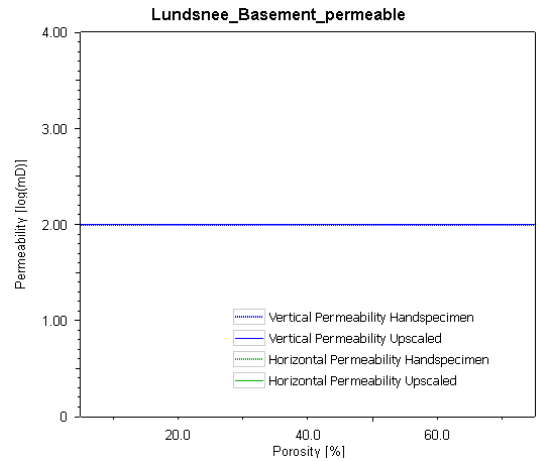


Fig. 13: Figure 2.12 from Zoback (2010) Default compaction curve for PetroMod’s “Shale (typical)” lithology. This compaction curve was used for the tested reservoir interval and all overburden in all 3D experiments here.

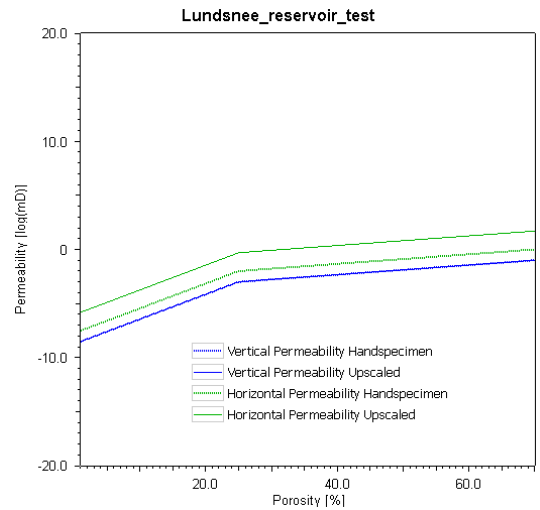
paction and permeability values for the “Shale (typical)” lithology (Figure 14b). A second and third run tested the effects of setting the overburden and underburden to impermeable and highly permeable values (Figure 14c), respectively. After completing each simulation, I extracted a vertical 1D profile from the center of the model to evaluate the evolution with time of P_p and ϕ at that point. Initial model conditions are tabulated in Appendix D. Petroleum migration modeling was disabled for these model runs because no hydrocarbons were produced. Two simulation cycles were conducted by PetroMod for each test in this experiment.

C. Experiment 3: Effect of compaction and fluid pressure increase from petroleum maturation in 3D

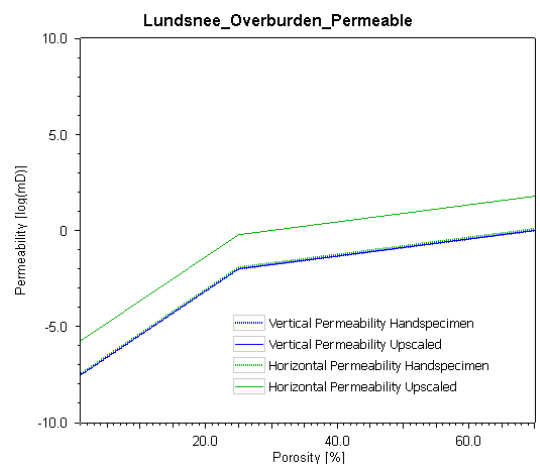
For Experiment 3, I again used the basic 3D model employed in Experiment 2, but this time tested the effects of pore fluid volume expansion during hydrocarbon maturation. To ensure sufficient levels of petroleum generation, I added high levels of total organic carbon (TOC = 20%) and hydrogen index (HI = 500 mgHC gTOC⁻¹) in the reservoir unit, with TII (Paris Basin) kinetics by Behar et al. (1997). Initial model conditions are tabulated in Appendix D. Hybrid (Darcy + Flowpath) migration was enabled for this experiment and only 1 simulation run was conducted by PetroMod for each test in this experiment. The first test assumed completely



(a) High-permeability case basement.



(b) Overburden k curve for default (moderate) permeability case. This is also the default permeability for the tested reservoir interval in all experiment runs.



(c) Overburden k curve for high permeability case.

Fig. 14: Permeability (k) curves for the lithologies with nonzero permeabilities tested in the 3D experiments.


impermeable overburden and underburden. In the second test, I employed high permeability values for the underburden (Figure 14a) and overburden (Figure 14c), keeping all other parameters the same.

D. Experiment 4: Effect of compaction and fluid pressure increase with superimposed compression in 3D

For Experiment 4, I once more employed the 3D “layercake” model shown in Figure 10 and again allowed petroleum generation to occur using the same parameters as in Experiment 3. However, during this experiment, I also imposed tectonic boundary conditions on the model, resulting in 1 km of compression during the entire model run. I conducted this experiment for both highly permeable (Figure 14c) and completely impermeable overburden and underburden strata. Initial model conditions are tabulated in Appendix D. Hybrid (Darcy + Flowpath) migration was enabled and only 1 simulation run was conducted by PetroMod for each test. The first test assumed impermeable overburden and underburden. In the second test, I employed high permeability values for the underburden (Figure 14a) and overburden (Figure 14c), keeping all other parameters the same.

IV. RESULTS

A. Experiment 1: Effect of loading and unloading in 1D

Experiment 1 applied sediment loading and unloading to a “reservoir” unit in 1D in order to match isotropic loading and unloading during a rock compression laboratory experiment reported by Zimmer (2004) and Zimmer et al. (2007b). Results of my replicated experiment are shown in Figure 15. During this BPSM experiment, pore pressure appears to have been roughly proportional to overburden stress imposed by sediment loading. Porosity, on the other hand, decreased in an unrecoverable manner  with every increase in overburden stress. Elastic porosity recovery was not observed.

B. Experiment 2: Effect of simple compaction in 3D

This 3D experiment tested a basic scenario in which a “reservoir” unit was loaded sequentially by 8 overburden units. Results are shown in Figure 16. During the first

run of this experiment, the overburden and underburden were set to default permeability values (impermeable underburden, moderately permeable overburden), resulting in the burial history shown in Figure 17a. Porosity decreased asymptotically during loading, approaching 6% (Figure 16a). Pore pressure appears to have been significantly below the set fracture gradient (see Figure 12) for the entire simulation.

During the second run, the overburden and underburden were completely impermeable, resulting in the burial history shown in Figure 17b. Reservoir porosity evolved in a curious manner; ϕ decreased beginning around 80 Ma, as in the first run, but only decreased by ca. 0.05% before stalling at a constant and very high value of ca. 44.55% for the remainder of the simulation (Figure 16b). For the majority of this simulation, P_p was extremely high, reaching > 150 MPa by the end of the run, which exceeded the set fracture gradient (Figure 16b). Overpressure magnitudes in excess of 40 MPa were observed at 0 Ma. During this run, the fracture pressure was highest at a given time compared with the other two runs, which is probably due to the large depth differences between the reservoirs in each run as a result of different compressibilities employed.

During a third run, the overburden permeability was set to high values (Figure 14c), resulting in the burial plot shown in Figure 17c. During this run, ϕ again decreased in an asymptotic manner, except that it reached values even lower than those attained during the moderate- k first run (*c.f.* Figures 16a and 16c). As in the first run, P_p remained well below the fracture gradient.

C. Experiment 3: Effect of compaction and fluid pressure increase from petroleum maturation in 3D

For this experiment, TOC and HI values were set to sufficiently high values in the “reservoir” unit that significant petroleum maturation occurred during simulation. The evolution of key parameters for all runs of this experiment were calculated for 1D extractions from the center of the model and are plotted in Figure 18.

The “base case” first run employed completely impermeable underburden and overburden (Figure 19). Petroleum maturation took place as burial proceeded, as

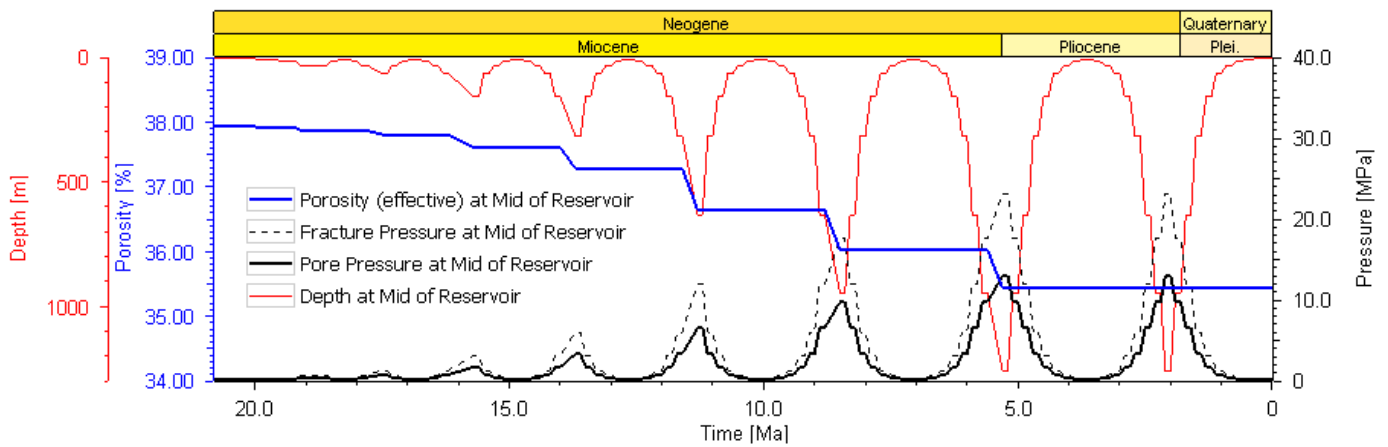


Fig. 15: Cluttered plot showing results from Experiment 1 versus time. Black curve reports ϕ and blue curve reports P_p during depth (σ) cycles shown by the red curve. The lack of increase for ϕ values during unloading (“erosion”) cycles clearly shows that PetroMod does not account for elastic rebound of porosity that is shown in rock physics experiments (Figures 1 and 6).

shown by increasing vitrinite reflectance ($\%R_o$) values. As in the second (impermeable strata) run of Experiment 2, the first porosity loss occurred at ca. 80 Ma, but porosity loss quickly ceased (Figure 18a). Intriguingly, ϕ was higher at the start of this run than in the impermeable strata (second) run of Experiment 2 (*c.f.* Figures 16b and 18a), and ϕ remained higher in this run. In contrast, P_p was lower during this run compared with the second run of Experiment 2.

During the second run, the overburden and underburden strata were assigned high permeability values (Figures 14 and 19b). As in the high- k (third) run of Experiment 2, ϕ decreased asymptotically to a low value of ca. 4% (Figure 18a). In addition, P_p remained far below the fracture pressure throughout burial. Petroleum maturation did not proceed as far during this run as in the first run (impermeable strata) of this experiment (*c.f.* Figures 18a and 18b). Unlike with Experiment 2, the fracture pressure remained approximately the same between the first (impermeable overburden) and second (permeable overburden) runs. This is probably because the reservoir maintained approximately identical depths with time during both runs as a result of the overburden having the same compaction curve.

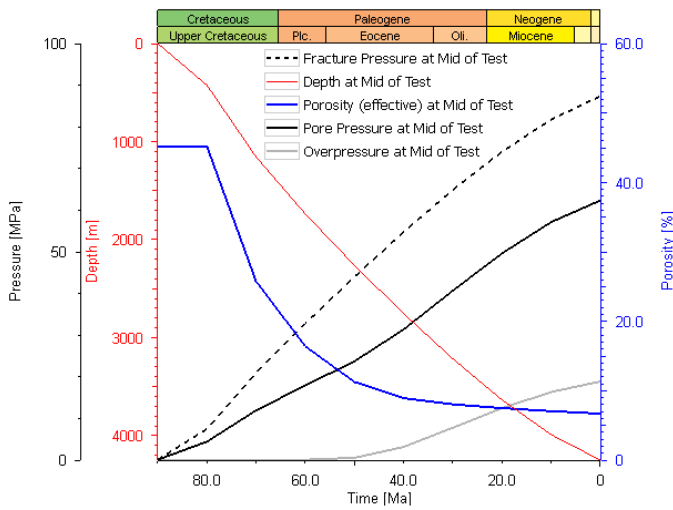
D. Experiment 4: Effect of compaction and fluid pressure increase with superimposed compression in 3D

Both runs of this experiment applied the same conditions as in Experiment 3, except that a compressional

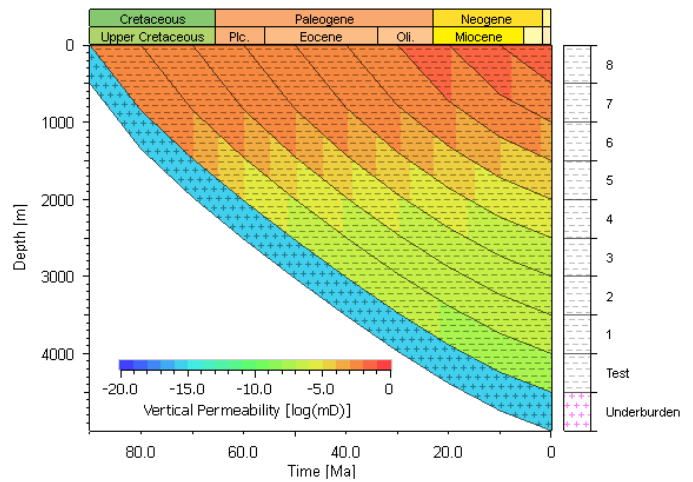
boundary condition (1000 m of shortening in both the N–S and E–W directions) was imposed during the course of model simulation. The evolution of key variables with time in a 1D profile extracted from the center of the model after each run is shown in Figure 20.

As in Experiment 3, overburden and underburden strata were impermeable during the first run of this experiment (Figure 21a). This resulted in very little porosity loss, all of which occurred at ca. 80 Ma (Figure 20a). Porosity remained constant at ca. 52.455% for the remainder of the simulation. Reservoir P_p exceeded the fracture pressure for most of the simulation. Interestingly, during these modeling conditions, $\%R_o$ reached 5%, its highest value in any of the modeling runs, and this value was attained early (ca. 50 Ma).

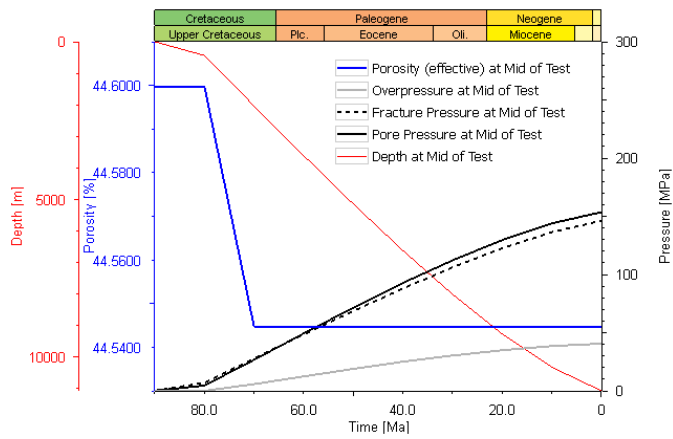
During the second run, the overburden and underburden were given high k values (Figure 21b). As a result, P_p remained far below the fracture pressure, never exceeding 65 MPa (Figure 20b). In contrast to the first (impermeable strata) run of this experiment, $\%R_o$ increased slowly and never reached 3%. Unlike with Experiment 3, the fracture pressure was higher at any time during the first (impermeable overburden) run. This appears to have resulted from different compaction histories between the first and second runs, as a result of their differing overburden characteristics and different reservoir compaction resulting from the extremely high P_p attained during the first run (Figure 20a).



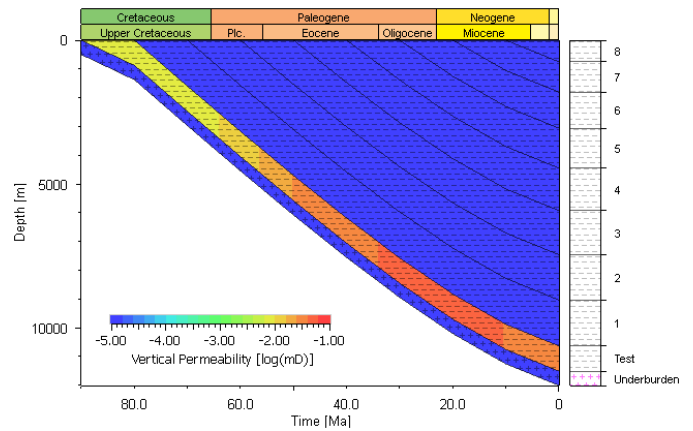
(a) Default k for overburden and underburden.



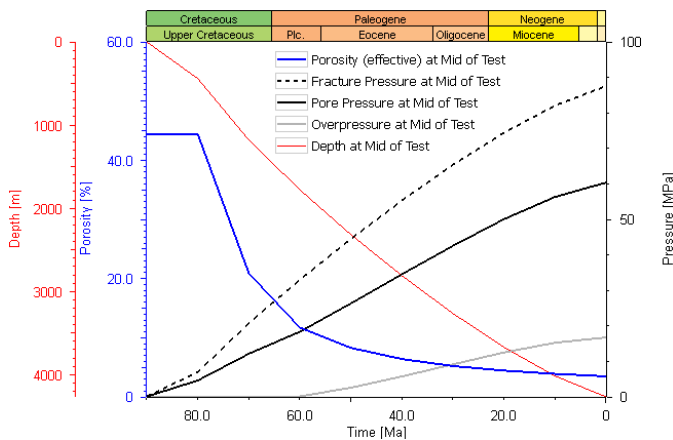
(a) Default k for overburden and underburden.



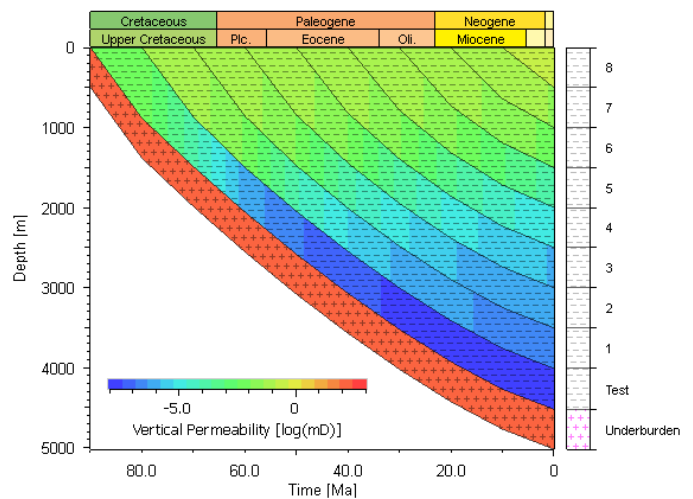
(b) Completely impermeable overburden and underburden.



(b) Completely impermeable overburden and underburden.



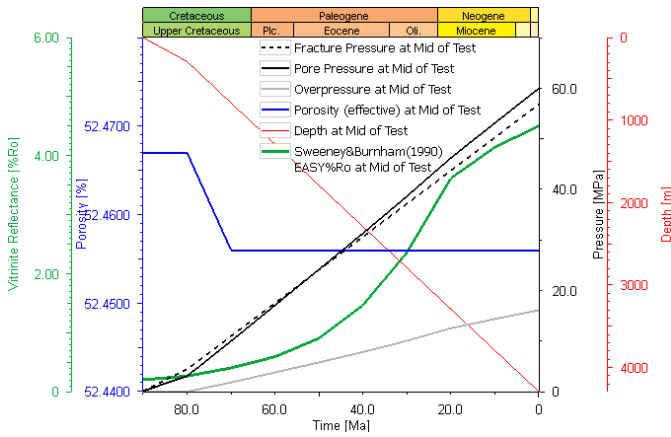
(c) High- k underburden and overburden (see Figures 14a and 14c).



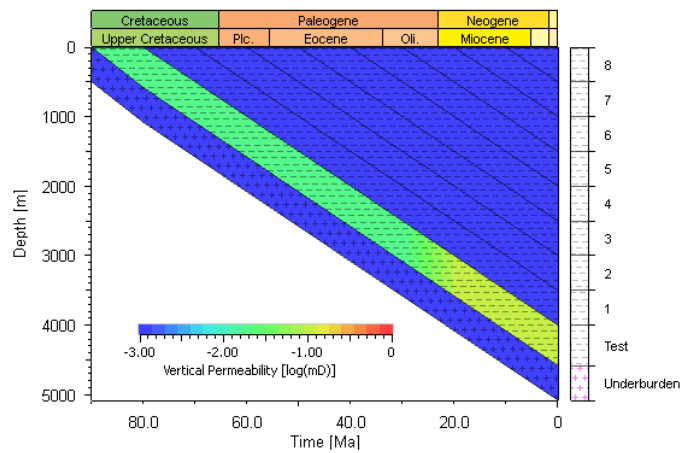
(c) High- k underburden and overburden (see Figures 14a and 14c).

Fig. 16: Results of Experiment 2 versus time. Burial depth is represented by the red curve, which shows depth to the center of the tested “reservoir” unit.

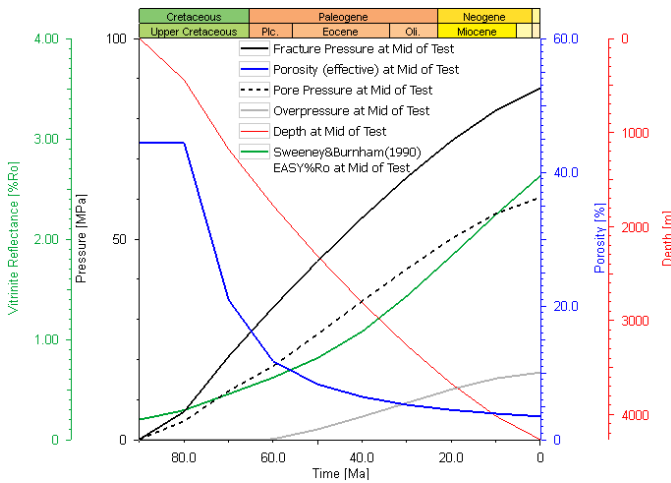
Fig. 17: Burial depth versus time for all strata deposited in Experiment 2. Color scale represents vertical permeability.



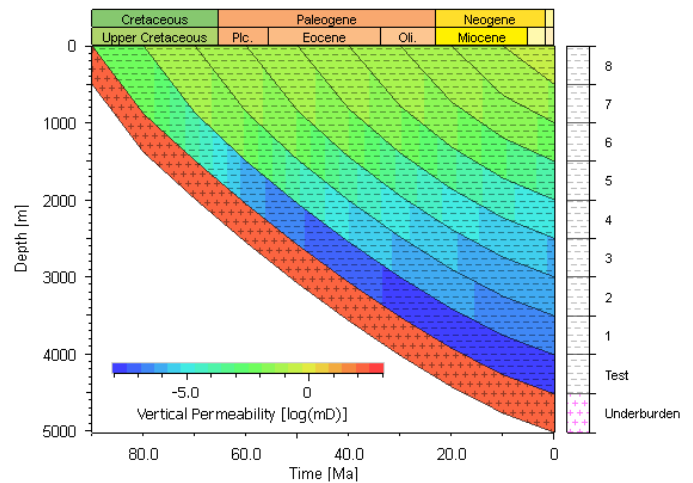
(a) Completely impermeable overburden and underburden.



(a) Completely impermeable overburden and underburden.



(b) High-*k* underburden and overburden (see Figures 14a and 14c).



(b) High-*k* underburden and overburden (see Figures 14a and 14c).

Fig. 18: Results of Experiment 3 versus time. Burial depth is represented by the red curve, which shows depth to the stratigraphic middle of the “reservoir” unit.

Fig. 19: Burial depth versus time for all strata deposited in Experiment 3. Color scale represents vertical permeability.

V. DISCUSSION AND CONCLUSIONS

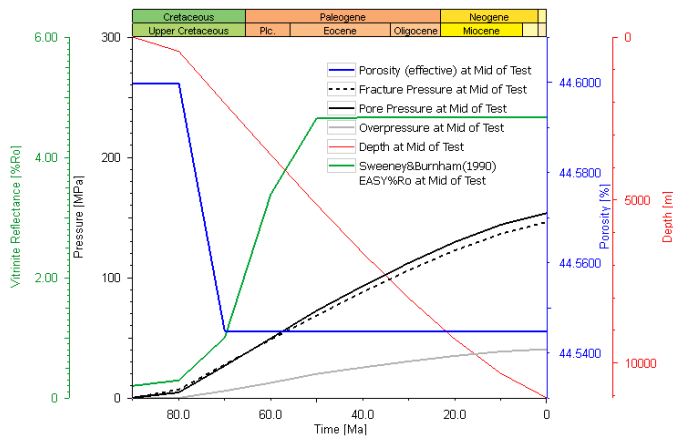
The central question of this term paper is whether BPSM provides unique capabilities for predicting overpressure in the subsurface that rival traditional geophysical inversion techniques. The experiments described above show the impressive capabilities of PetroMod BPSM software for this application, as well as some notable limitations for understanding the evolution of P_p , stress, and ϕ in the subsurface. The results also reveal important characteristics of basin and petroleum systems evolution, PetroMod’s algorithms, or both.

During Experiment 1, I replicated laboratory rock compression results reported by Zimmer (2004) and Zimmer et al. (2007b), which are shown in Figure 6. The results highlight an important limitation of the

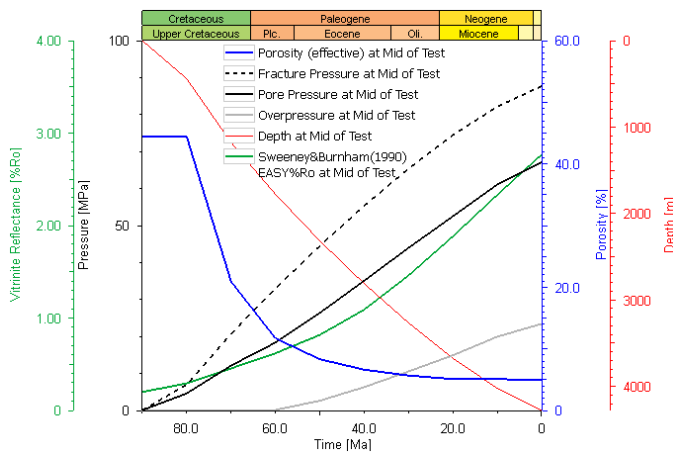
software that has significant implications for drilling and hydrocarbon exploration: the inability to model elastic rebound during reductions in σ results in erroneous predictions for ϕ , which could lead to underestimation of the size of a pressure hazard at depth or underprediction of hydrocarbon volumes in place at a prospect.

Nevertheless, these results show that the software is able to model significant fluctuations in P_p even as ϕ remains constant. This provides a clear advantage over seismic inversion techniques that predict overpressure through detection of abnormally elevated ϕ (see discussion in Dutta, 2002; Chopra and Huffman, 2006; Gutierrez et al., 2006; Zhang, 2011).

Experiments 2–4 likewise illustrate the power of BPSM for estimating P_p at depth, particularly in cases



(a) Completely impermeable overburden and underburden.

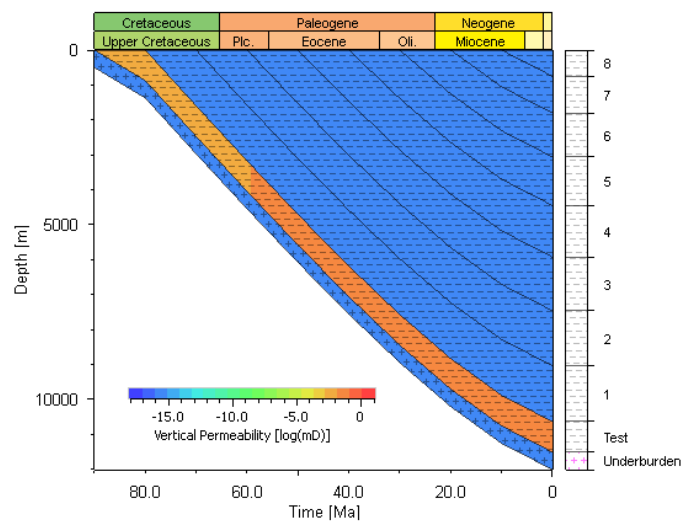


(b) High-*k* underburden and overburden (see Figures 14a and 14c).

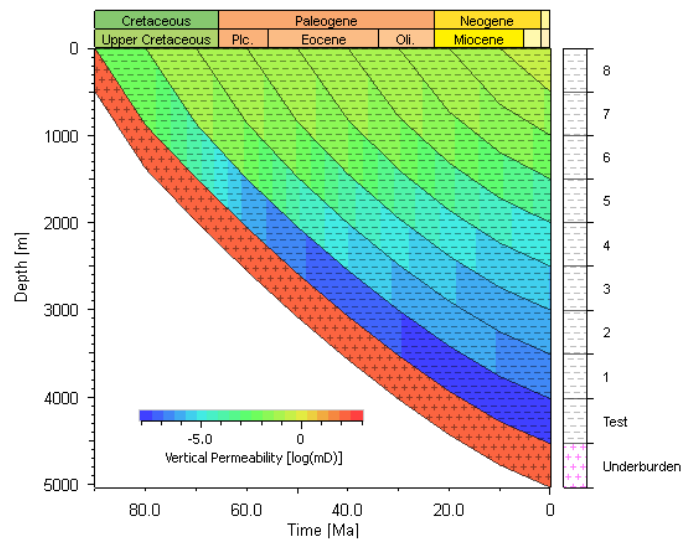
Fig. 20: Results of Experiment 4 versus time. Burial depth is represented by the red curve, which shows depth to the stratigraphic middle of the “reservoir” unit.

of low ϕ that might not indicate overpressure using geophysical methods that invert ϕ values. These experiments each compared the effects of changing the permeability of overburden and underburden in three simple scenarios for compaction in 3D.

In model runs employing permeable overburden and underburden, ϕ continues to decrease asymptotically (though probably at a diminished rate of porosity loss) as overpressure develops (Figures 16a, 16c, 18b, and 20b). This is not a surprising result; we expect ϕ to decrease asymptotically during compaction, and that it will decrease less quickly during overpressure development. However, these basin modeling results show that ϕ is not expected to increase dramatically as overpressure develops, in spite of the contrary expectation shown in cartoon fashion by Figure 3.



(a) Completely impermeable overburden and underburden.



(b) High-*k* underburden and overburden (see Figures 14a and 14c).

Fig. 21: Burial depth versus time for all strata deposited in Experiment 4. Color scale represents vertical permeability.

Instead, these results show that BPSM provides a means for quantifying ϕ and P_p , allowing us to detect elevated P_p even in the subtle cases shown here, where only the gradient of ϕ decrease changes with overpressure. PetroMod can account well for nonrecoverable porosity loss and can easily employ custom compaction parameters. Thus, the program can provide meaningful estimates for P_p and could even act as a calibration tool for geophysical overpressure detection methods.

The results of model runs in which overburden and underburden were impermeable likewise illustrate some important remaining limitations of BPSM for use in

estimating overpressure. During these runs, the reservoir attained high degrees of overpressure (Figures 16b, 18a, and 20a). In all of these cases, P_p was high enough that it exceeded the fracture pressure during the simulation.

This result is also not particularly surprising. What is more interesting is that in all of these cases k changed little and ϕ remained nearly constant during the entire simulation. In each case, ϕ decreased early during loading, as would be expected, but then remained constant between ca. 70–0 Ma (Figures 16b, 18a, and 20a). This unexpected compaction pattern appears to be an artifact of the way PetroMod calculates ϕ in the presence of high overpressures (W. AIKawai, pers. comm.); in such cases, very high P_p completely prevents compaction, despite continued accumulation of overburden.

Of course, a more sophisticated model than that employed for experiments 2–4 (Figure 10) would account for a range of dynamic pore pressure controls, including fault-valve behaviors in the presence of elevated P_p (see, for example, Sibson and Scott, 1998; Townend and Zoback, 2000; Finkbeiner et al., 2001; Zoback and Townend, 2001; Sibson, 2003; Lund Snee et al., 2014; Burgreen-Chan et al., 2015).

In addition, it is challenging to confidently identify the mechanism explaining some differences between ϕ , P_p , k , and fracture pressure profiles produced during different tests (Figures 16, 17, 18, 19, 20, and 21). This suggests that additional factors besides the explicitly tested experimental variables may also contribute to these results. For example, we have seen that different lithological and, perhaps, P_p parameters resulted in different degrees of overburden compaction, which in turn resulted in different reservoir burial depths with time in different tests. This situation probably therefore introduced additional, untested variables into the simulations. Future tests of sophisticated BPSM software should be designed more carefully than done here, in such a way that unintended variables are not unknowingly introduced into a model. These tests should be conducted by someone having thorough understanding of the modeling algorithms employed by the software.

The peculiar lack of compaction in the presence of high P_p illustrates a basic limitation of using basin mod-

eling software as an independent measure of overpressure: nonphysical results may easily occur if adequate parameters and processes are not employed in the model, and it can be difficult to detect errors or understand their origin due to the typical complexity of the models and modeling algorithms.

In addition, in these experimental runs k continued to decrease slightly even after constant ϕ was achieved (see Figures 17b, 19a, and 21a). During Experiment 2 (basic compaction with neither petroleum generation nor tectonic compression), k actually increased slightly after 10 Ma, near the end of burial (Figure 17b). This result was quite unexpected and could perhaps have resulted from modeled fracturing of the reservoir interval as a result of P_p in excess of the fracture pressure. However, this proposed explanation does not adequately account for the slight loss of k during the last ca. 10 Ma of the second (impermeable overburden and underburden) run of Experiment 2 (16b).

Despite these apparently nonphysical results, a tremendous advantage of BPSM as a tool for predicting P_p at depth is that its estimates can be completely independent from sonic velocity and density measurements. A major benefit of using BPSM for this purpose arises from the observation that P_p is able to change semi-independently of ϕ under certain circumstances.

Because geologic history, present-day basin geometries, stratigraphy, and thermal and rock physics parameters are the dominant inputs for BPSM studies, this method has great potential to act, at the least, as a check on other techniques. As BPSM capabilities continue to improve, our understanding of rock physics and geology will increasingly become our greatest limitations.

VI. ACKNOWLEDGMENTS

Allegra Hosford Scheirer of Stanford University and Noelle Schoellkopf of Schlumberger provided me with a great deal of assistance and advice for formulating a research question and building an appropriate basin model. I appreciate their interest in this project. Wisam AIKawai and Yao Tong of Stanford helped set me straight about methods for modeling pore pressure evolution and erosion in PetroMod. I am also grateful to Uri Wollner of Stanford for helpful discussions about elastic recovery in sedimentary rocks and for pointing me toward Michael Zimmer's research.

REFERENCES

- Al-Hajeri, M.M., and Al Saeed, M., 2009, Basin and Petroleum System Modeling: *Oilfield Review*, v. 21, no. 7, p. 14–29, URL http://www.slb.com/resources/publications/industry_articles/oilfield_review/2009/or2009sum02_basin_and_petroleum.aspx.
- Athy, L.F., 1930, Density, porosity, and compaction of sedimentary rocks: *AAPG Bulletin*, v. 14, no. 1, p. 1–24.
- Behar, F., Vandenbroucke, M., Tang, Y., Marquis, F., and Espitalie, J., 1997, Thermal cracking of kerogen in open and closed systems: determination of kinetic parameters and stoichiometric coefficients for oil and gas generation: *Organic Geochemistry*, v. 26, no. 5, p. 321–339, doi:10.1016/S0146-6380(97)00014-4.
- Biot, M.A., 1941, General theory of three-dimensional consolidation: *Journal of Applied Physics*, v. 12, no. 2, p. 155–164, doi:10.1063/1.1712886.
- Bowers, G.L., 2002, Detecting high overpressure: *The Leading Edge*, v. 21, no. 2, p. 174, doi:10.1190/1.1452608.
- Burgreen-Chan, B., Meisling, K.E., and Graham, S., 2015, Basin and petroleum system modelling of the East Coast Basin, New Zealand: a test of overpressure scenarios in a convergent margin: *Basin Research*, p. 1–32, doi:10.1111/bre.12121.
- Byerlee, J., 1978, Friction of rocks: *Pure and applied geophysics*, v. 116, no. 4-5, p. 615–626.
- Carman, P.C., 1956, *Flow of gases through porous media*: Butterworths Scientific Publications London.
- Chopra, S., and Huffman, A.R., 2006, Velocity determination for pore-pressure prediction: *The Leading Edge*, v. 25, no. 12, p. 1502, doi:10.1190/1.2405336.
- Dutta, N.C., 2002, Geopressure prediction using seismic data: Current status and the road ahead: *Geophysics*, v. 67, no. 6, p. 2012, doi:10.1190/1.1527101.
- Finkbeiner, T., Zoback, M., Flemings, P., Stump, B., and Finkbeiner, T., 2001, Stress, pore pressure, and dynamically constrained hydrocarbon columns in the South Eugene Island 330 field, northern Gulf of Mexico: *AAPG bulletin*, v. 85, no. 6, p. 1007–1031.
- Gutierrez, M.a., Braunsdor, N.R., and Couzens, B.a., 2006, Calibration and ranking of pore-pressure prediction models: *The Leading Edge*, v. 25, no. 12, p. 1516, doi:10.1190/1.2405337.
- Hantschel, T., and Kauerauf, A.I., 2009, *Fundamentals of basin and petroleum systems modeling*: Springer Science & Business Media.
- Lund Snee, J.E., Toy, V.G., and Gessner, K., 2014, Significance of brittle deformation in the footwall of the Alpine Fault, New Zealand: Smithy Creek Fault zone: *Journal of Structural Geology*, v. 64, p. 79–98, doi:10.1016/j.jsg.2013.06.002, URL <http://dx.doi.org/10.1016/j.jsg.2013.06.002>.
- Nur, A., and Byerlee, J.D., 1971, An exact effective stress law for elastic deformation of rock with fluids: *Journal of Geophysical Research*, v. 76, no. 26, p. 6414, doi:10.1029/JB076i026p06414.
- Peters, K.E., Schenk, O., Scheirer, A.H., Wygrala, B., and Hantschel, T., , Chapter x . *Basin and Petroleum System Modeling of Conventional and Unconventional Petroleum Resources*, p. 1–47.
- Sayers, C.M., Johnson, G.M., and Denyer, G., 2002, Predrill pore-pressure prediction using seismic data: *Geophysics*, v. 67, no. 4, p. 1286, doi:10.1190/1.1500391.
- Schlumberger, 2014a, *PetroMod Version 2014 -1 2D/3D Simulator User Guide*,
- Schlumberger, 2014b, *PetroMod Version 2014-1 Lithology Editor User Guide*,
- Sibson, R.H., and Scott, J., 1998, Stress/fault controls on the containment and release of overpressured fluids: examples from gold-quartz vein systems in Juneau, Alaska; Victoria, Australia and Otago, New Zealand: *Ore Geology Reviews*, v. 13, no. 1-5, p. 293–306, doi:10.1016/S0169-1368(97)00023-1.
- Sibson, R.H., 2003, Brittle-failure controls on maximum sustainable overpressure in different tectonic regimes: *AAPG Bulletin*, v. 87, no. 6, p. 901–908, doi:10.1306/01290300181.
- Sutherland, R., Toy, V.G., Townend, J., Cox, S.C., Eccles, J.D., Faulkner, D.R., Prior, D.J., Norris, R.J., Mariani, E., Boulton, C., Carpenter, B.M., Menzies, C.D., Little, T.a., Hasting, M., De Pascale, G.P., Langridge, R.M., Scott, H.R., Reid Lindroos, Z., Fleming, B., and Kopf, J., 2012, Drilling reveals fluid control on architecture and rupture of the Alpine fault, New Zealand: *Geology*, v. 40, no. 12, p. 1143–1146, doi:10.1130/G33614.1.
- Swarbrick, R.E., Osborne, M.J., and Yardley, G.S., 2002, Comparison of Overpressure Magnitude Resulting from the Main Generating Mechanisms: *AAPG Memoirs*, v. 76, p. 1–12.
- Townend, J., and Zoback, M.D., 2000, How faulting keeps the crust strong: *Geology*, v. 28, no. 5, p. 399–402, doi:10.1130/0091-7613(2000)28(399:HFKTCS)2.0.CO.
- von Terzaghi, K., 1923, Die berechnung der durchlassigkeitsziffer des tones aus dem verlauf der hydrodynamischen spannungsercheinungen: *Sitzungsberichte der Akademie der Wissenschaften in Wien, Mathematisch-Naturwissenschaftliche Klasse, Abteilung IIa*, v. 132, p. 125–138.
- Zhang, J., 2011, Pore pressure prediction from well logs: Methods, modifications, and new approaches: *Earth-Science Reviews*, v. 108, no. 1-2, p. 50–63, doi:10.1016/j.earscirev.2011.06.001.
- Zimmer, M.A., 2004, Seismic velocities in unconsolidated sands: Measurements of pressure, sorting, and compaction effects: URL <http://adsabs.harvard.edu/abs/2004PhDT.....417Z>.
- Zimmer, M.A., Prasad, M., and Mavko, G., 2002, Pressure and porosity influences on $V_{[sub P]}-V_{[sub S]}$ ratio in unconsolidated sands: *The Leading Edge*, v. 21, no. 2, p. 178, doi:10.1190/1.1452609.
- Zimmer, M.A., Prasad, M., Mavko, G., and Nur, A., 2007a, Seismic velocities of unconsolidated sands: Part 1 Pressure trends from 0.1 to 20 MPa: *Geophysics*, v. 72, no. 1, p. E1, doi:10.1190/1.2399459.
- Zimmer, M.A., Prasad, M., Mavko, G., and Nur, A., 2007b, Seismic velocities of unconsolidated sands: Part 2 Influence of sorting- and compaction-induced porosity variation: *Geophysics*, v. 72, no. 1, p. E15, doi:10.1190/1.2364849.
- Zoback, M.D., 2010, *Reservoir geomechanics*: Cambridge University Press.
- Zoback, M.D., and Townend, J., 2001, Implications of hydrostatic pore pressures and high crustal strength for the deformation of intraplate lithosphere: *Tectonophysics*, v. 336, p. 19–30, doi:10.1016/S0040-1951(01)00091-9.

Appendix B: Data used for Experiment 1 burial history input
 Jens-Erik Lund Sneek

Name	Lithology	Density at deposition kg m ⁻³	Thickness of overburden m	Thickness of unit	Depositional start Ma	Depositional end Ma	Pressure Mpa	Porosity 0.3794	Additional overburden Mpa	
103	Overburden	Perfect seal	1617	0	-3.155250969	0.2	0.1	0	0.3544	-0.05
102	Overburden	Perfect seal	1617	3.155250969	-3.155250969	0.4	0.3	0.05	0.3479	-0.05
101	Overburden	Perfect seal	1617	6.310501937	-6.310501937	0.6	0.5	0.1	0.346	-0.1
100	Overburden	Perfect seal	1617	12.62100387	-18.93150581	0.8	0.7	0.2	0.3444	-0.3
99	Overburden	Perfect seal	1617	31.55250969	-31.55250969	1	0.9	0.5	0.3424	-0.5
98	Overburden	Perfect seal	1617	63.10501937	-94.65752906	1.2	1.1	1	0.3408	-1.5
97	Overburden	Perfect seal	1617	157.7625484	-157.7625484	1.4	1.3	2.5	0.3385	-2.5
96	Overburden	Perfect seal	1617	315.5250969	-315.5250969	1.6	1.5	5	0.3365	-5
95	Overburden	Perfect seal	1617	631.0501937	-315.5250969	1.8	1.7	10	0.334	-5
94	Overburden	Perfect seal	1617	946.5752906	-315.5250969	2	1.9	15	0.3326	-5
93	Overburden	Perfect seal	1617	1262.100387	315.5250969	2.2	2.1	20	0.3315	5
92	Overburden	Perfect seal	1617	946.5752906	315.5250969	2.4	2.3	15	0.3349	5
91	Overburden	Perfect seal	1617	631.0501937	315.5250969	2.6	2.5	10	0.3376	5
90	Overburden	Perfect seal	1617	315.5250969	157.7625484	2.8	2.7	5	0.3408	2.5
89	Overburden	Perfect seal	1617	157.7625484	94.65752906	3	2.9	2.5	0.3433	1.5
88	Overburden	Perfect seal	1617	63.10501937	31.55250969	3.2	3.1	1	0.3458	0.5
87	Overburden	Perfect seal	1617	31.55250969	18.93150581	3.4	3.3	0.5	0.3474	0.3
86	Overburden	Perfect seal	1617	12.62100387	6.310501937	3.6	3.5	0.2	0.3487	0.1
85	Overburden	Perfect seal	1617	6.310501937	-6.310501937	3.8	3.7	0.1	0.3492	-0.1
84	Overburden	Perfect seal	1617	12.62100387	-18.93150581	4	3.9	0.2	0.348	-0.3
83	Overburden	Perfect seal	1617	31.55250969	-31.55250969	4.2	4.1	0.5	0.3458	-0.5
82	Overburden	Perfect seal	1617	63.10501937	-94.65752906	4.4	4.3	1	0.3444	-1.5
81	Overburden	Perfect seal	1617	157.7625484	-157.7625484	4.6	4.5	2.5	0.3419	-2.5
80	Overburden	Perfect seal	1617	315.5250969	-315.5250969	4.8	4.7	5	0.3398	-5
79	Overburden	Perfect seal	1617	631.0501937	-315.5250969	5	4.9	10	0.3375	-5
78	Overburden	Perfect seal	1617	946.5752906	-315.5250969	5.2	5.1	15	0.336	-5
77	Overburden	Perfect seal	1617	1262.100387	157.7625484	5.4	5.3	20	0.3349	2.5
76	Overburden	Perfect seal	1617	1104.337839	157.7625484	5.6	5.5	17.5	0.338	2.5
75	Overburden	Perfect seal	1617	946.5752906	315.5250969	5.8	5.7	15	0.3399	5
74	Overburden	Perfect seal	1617	631.0501937	315.5250969	6	5.9	10	0.3437	5
73	Overburden	Perfect seal	1617	315.5250969	157.7625484	6.2	6.1	5	0.3473	2.5
72	Overburden	Perfect seal	1617	157.7625484	94.65752906	6.4	6.3	2.5	0.3497	1.5
71	Overburden	Perfect seal	1617	63.10501937	31.55250969	6.6	6.5	1	0.3523	0.5
70	Overburden	Perfect seal	1617	31.55250969	18.93150581	6.8	6.7	0.5	0.3538	0.3
69	Overburden	Perfect seal	1617	12.62100387	6.310501937	7	6.9	0.2	0.3552	0.1
68	Overburden	Perfect seal	1617	6.310501937	-6.310501937	7.2	7.1	0.1	0.3556	-0.1
67	Overburden	Perfect seal	1617	12.62100387	-18.93150581	7.4	7.3	0.2	0.3544	-0.3
66	Overburden	Perfect seal	1617	31.55250969	-31.55250969	7.6	7.5	0.5	0.3525	-0.5
65	Overburden	Perfect seal	1617	63.10501937	-94.65752906	7.8	7.7	1	0.3508	-1.5
64	Overburden	Perfect seal	1617	157.7625484	-157.7625484	8	7.9	2.5	0.3485	-2.5
63	Overburden	Perfect seal	1617	315.5250969	-315.5250969	8.2	8.1	5	0.3464	-5
62	Overburden	Perfect seal	1617	631.0501937	-315.5250969	8.4	8.3	10	0.344	-5
61	Overburden	Perfect seal	1617	946.5752906	157.7625484	8.6	8.5	15	0.3426	2.5
60	Overburden	Perfect seal	1617	788.8127422	157.7625484	8.8	8.7	12.5	0.346	2.5
59	Overburden	Perfect seal	1617	631.0501937	315.5250969	9	8.9	10	0.349	5
58	Overburden	Perfect seal	1617	315.5250969	157.7625484	9.2	9.1	5	0.354	2.5
57	Overburden	Perfect seal	1617	157.7625484	94.65752906	9.4	9.3	2.5	0.3567	1.5
56	Overburden	Perfect seal	1617	63.10501937	31.55250969	9.6	9.5	1	0.3591	0.5
55	Overburden	Perfect seal	1617	31.55250969	18.93150581	9.8	9.7	0.5	0.3604	0.3
54	Overburden	Perfect seal	1617	12.62100387	6.310501937	10	9.9	0.2	0.3618	0.1
53	Overburden	Perfect seal	1617	6.310501937	-6.310501937	10.2	10.1	0.1	0.3621	-0.1
52	Overburden	Perfect seal	1617	12.62100387	-18.93150581	10.4	10.3	0.2	0.3611	-0.3
51	Overburden	Perfect seal	1617	31.55250969	-31.55250969	10.6	10.5	0.5	0.3594	-0.5
50	Overburden	Perfect seal	1617	63.10501937	-94.65752906	10.8	10.7	1	0.3579	-1.5
49	Overburden	Perfect seal	1617	157.7625484	-157.7625484	11	10.9	2.5	0.3556	-2.5
48	Overburden	Perfect seal	1617	315.5250969	-315.5250969	11.2	11.1	5	0.3536	-5
47	Overburden	Perfect seal	1617	631.0501937	157.7625484	11.4	11.3	10	0.3514	2.5
46	Overburden	Perfect seal	1617	473.2876453	157.7625484	11.6	11.5	7.5	0.3558	2.5
45	Overburden	Perfect seal	1617	315.5250969	157.7625484	11.8	11.7	5	0.3601	2.5
44	Overburden	Perfect seal	1617	157.7625484	94.65752906	12	11.9	2.5	0.3635	1.5
43	Overburden	Perfect seal	1617	63.10501937	31.55250969	12.2	12.1	1	0.3661	0.5
42	Overburden	Perfect seal	1617	31.55250969	18.93150581	12.4	12.3	0.5	0.3675	0.3
41	Overburden	Perfect seal	1617	12.62100387	6.310501937	12.6	12.5	0.2	0.3686	0.1
40	Overburden	Perfect seal	1617	6.310501937	-6.310501937	12.8	12.7	0.1	0.3688	-0.1
39	Overburden	Perfect seal	1617	12.62100387	-18.93150581	13	12.9	0.2	0.3681	-0.3
38	Overburden	Perfect seal	1617	31.55250969	-31.55250969	13.2	13.1	0.5	0.3665	-0.5
37	Overburden	Perfect seal	1617	63.10501937	-94.65752906	13.4	13.3	1	0.3651	-1.5
36	Overburden	Perfect seal	1617	157.7625484	-157.7625484	13.6	13.5	2.5	0.363	-2.5
35	Overburden	Perfect seal	1617	315.5250969	78.88127422	13.8	13.7	5	0.3612	1.25
34	Overburden	Perfect seal	1617	236.6438226	78.88127422	14	13.9	3.75	0.3641	1.25
33	Overburden	Perfect seal	1617	157.7625484	94.65752906	14.2	14.1	2.5	0.3665	1.5
32	Overburden	Perfect seal	1617	63.10501937	31.55250969	14.4	14.3	1	0.3697	0.5
31	Overburden	Perfect seal	1617	31.55250969	18.93150581	14.6	14.5	0.5	0.3711	0.3
30	Overburden	Perfect seal	1617	12.62100387	6.310501937	14.8	14.7	0.2	0.3721	0.1
29	Overburden	Perfect seal	1617	6.310501937	-6.310501937	15	14.9	0.1	0.3723	-0.1
28	Overburden	Perfect seal	1617	12.62100387	-18.93150581	15.2	15.1	0.2	0.3716	-0.3
27	Overburden	Perfect seal	1617	31.55250969	-31.55250969	15.4	15.3	0.5	0.3702	-0.5
26	Overburden	Perfect seal	1617	63.10501937	-94.65752906	15.6	15.5	1	0.369	-1.5
25	Overburden	Perfect seal	1617	157.7625484	31.55250969	15.8	15.7	2.5	0.3673	0.5
24	Overburden	Perfect seal	1617	126.2100387	31.55250969	16	15.9	2	0.3687	0.5
23	Overburden	Perfect seal	1617	94.65752906	31.55250969	16.2	16.1	1.5	0.3702	0.5
22	Overburden	Perfect seal	1617	63.10501937	31.55250969	16.4	16.3	1	0.3718	0.5
21	Overburden	Perfect seal	1617	31.55250969	18.93150581	16.6	16.5	0.5	0.3736	0.3
20	Overburden	Perfect seal	1617	12.62100387	6.310501937	16.8	16.7	0.2	0.3744	0.1
19	Overburden	Perfect seal	1617	6.310501937	-6.310501937	17	16.9	0.1	0.3748	-0.1
18	Overburden	Perfect seal	1617	12.62100387	-18.93150581	17.2	17.1	0.2	0.3742	-0.3
17	Overburden	Perfect seal	1617	31.55250969	-31.55250969	17.4	17.3	0.5	0.3731	-0.5
16	Overburden	Perfect seal	1617	63.10501937	15.77625484	17.6	17.5	1	0.3723	0.25
15	Overburden	Perfect seal	1617	47.32876453	15.77625484	17.8	17.7	0.75	0.3735	0.25
14	Overburden	Perfect seal	1617	31.55250969	18.93150581	18	17.9	0.5	0.3747	0.3
13	Overburden	Perfect seal	1617	12.62100387	6.310501937	18.2	18.1	0.2	0.3758	0.1
12	Overburden	Perfect seal	1617	6.310501937	-6.310501937	18.4	18.3	0.1	0.3761	-0.1
11	Overburden	Perfect seal	1617	12.62100387	-18.93150581	18.6	18.5	0.2	0.3755	-0.3
10	Overburden	Perfect seal	1617	31.55250969	11.98995368	18.8	18.7	0.5	0.375	0.19

9 Overburden Perfect seal	1617	19.56255601	6.941552131	19	18.9	0.31	0.3762	0.11
8 Overburden Perfect seal	1617	12.62100387	6.310501937	19.2	19.1	0.2	0.377	0.1
7 Overburden Perfect seal	1617	6.310501937	-6.310501937	19.4	19.3	0.1	0.3772	-0.1
6 Overburden Perfect seal	1617	12.62100387	3.155250969	19.6	19.5	0.2	0.3769	0.05
5 Overburden Perfect seal	1617	9.465752906	3.155250969	19.8	19.7	0.15	0.3776	0.05
4 Overburden Perfect seal	1617	6.310501937	1.577625484	20	19.9	0.1	0.3782	0.025
3 Overburden Perfect seal	1617	4.732876453	1.577625484	20.2	20.1	0.075	0.3785	0.025
2 Overburden Perfect seal	1617	3.155250969	1.514520465	20.4	20.3	0.05	0.3789	0.024
1 Overburden Perfect seal	1617	1.640730504	1.640730504	20.6	20.5	0.026	0.3791	0.026
Reservoir	1617	300	1	20.8	20.7	0	0.3794	
Underburden Noncompressible, perfect seal	1617	1000	10	60	50			

Appendix C: Custom compaction curve for test lithology in Experiment 1

Based on values reported by Zimmer (2003) for sample "SC 35% Small"

Jens-Erik Lund Snee

<u>Porosity</u>	<u>Effective stress (MPa)</u>
37.94	0
37.91	0.03
37.89	0.05
37.85	0.08
37.82	0.1
37.76	0.15
37.69	0.2
37.5	0.5
37.23	1
36.73	2.5
36.12	5
35.14	10
34.26	15
33.49	20
32.47	26.56
31.18	35.84
30.59	40.39
30.34	42.5
29.99	45
29.64	47.5
29.31	50
28.98	52.5
28.66	55
28.35	57.5
28.04	60
27.74	62.5
27.45	65
27.17	67.5
26.9	70
26.63	72.5
26.36	75

Appendix D: PetroMod age assignment and facies definition tables for 3D experiments

Jens-Erik lund Snee

Experiment 2a:

Age (Ma)	Horizon	Depth Map	Layer	Event Type	Facies Map	No. of Sublayers	Max. Time Step (Ma)
0	Top_8	Horizon_0		8 Deposition	Overburden_Map	1	10
10	Top_7	Horizon_10		7 Deposition	Overburden_Map	1	10
20	Top_6	Horizon_20		6 Deposition	Overburden_Map	1	10
30	Top_5	Horizon_30		5 Deposition	Overburden_Map	1	10
40	Top_4	Horizon_40		4 Deposition	Overburden_Map	1	10
50	Top_3	Horizon_50		3 Deposition	Overburden_Map	1	10
60	Top_2	Horizon_60		2 Deposition	Overburden_Map	1	10
70	Top_1	Horizon_70		1 Deposition	Overburden_Map	1	10
80	Top_Test	Horizon_80	Test	Deposition	Test_Map	1	10
90	Top_Underburden	Horizon_90	Underburden	Deposition	Upper crust (continental, granite)_Facies_Map	1	10
100	Base_Underburden	Horizon_100					

Name	Lithology Value	TOC Mode	TOC Value (%)	Kinetics	HI Mode	HI Value (mgHC/gTOC)	Petroleum System Elements
Overburden	Shale (typical)						Overburden Rock
Test	Shale (typical)						Reservoir Rock
Upper crust (continental, granite)_Facies	Upper crust (continental, granite)						Underburden Rock

Experiment 2b:

Age (Ma)	Horizon	Depth Map	Layer	Event Type	Facies Map	No. of Sublayers	Max. Time Step (Ma)
0	Top_8	Horizon_0		8 Deposition	Overburden_Map	1	10
10	Top_7	Horizon_10		7 Deposition	Overburden_Map	1	10
20	Top_6	Horizon_20		6 Deposition	Overburden_Map	1	10
30	Top_5	Horizon_30		5 Deposition	Overburden_Map	1	10
40	Top_4	Horizon_40		4 Deposition	Overburden_Map	1	10
50	Top_3	Horizon_50		3 Deposition	Overburden_Map	1	10
60	Top_2	Horizon_60		2 Deposition	Overburden_Map	1	10
70	Top_1	Horizon_70		1 Deposition	Overburden_Map	1	10
80	Top_Test	Horizon_80	Test	Deposition	Test_Map	1	10
90	Top_Underburden	Horizon_90	Underburden	Deposition	Upper crust (continental, granite)_Facies_Map	1	10
100	Base_Underburden	Horizon_100					

Name	Lithology Value	TOC Mode	TOC Value (%)	Kinetics	HI Mode	HI Value (mgHC/gTOC)	Petroleum System Elements
Overburden	Lundsnee_Overburden_Sealing						Overburden Rock
Test	Lundsnee_reservoir_test						Reservoir Rock
Upper crust (continental, granite)_Facies	Lundsnee_Basement_sealing						Underburden Rock

Experiment 2c:

Age (Ma)	Horizon	Depth Map	Layer	Event Type	Facies Map	No. of Sublayers	Max. Time Step (Ma)
0	Top_8	Horizon_0		8 Deposition	Overburden_Map	1	10
10	Top_7	Horizon_10		7 Deposition	Overburden_Map	1	10
20	Top_6	Horizon_20		6 Deposition	Overburden_Map	1	10
30	Top_5	Horizon_30		5 Deposition	Overburden_Map	1	10
40	Top_4	Horizon_40		4 Deposition	Overburden_Map	1	10
50	Top_3	Horizon_50		3 Deposition	Overburden_Map	1	10
60	Top_2	Horizon_60		2 Deposition	Overburden_Map	1	10
70	Top_1	Horizon_70		1 Deposition	Overburden_Map	1	10
80	Top_Test	Horizon_80	Test	Deposition	Test_Map	1	10
90	Top_Underburden	Horizon_90	Underburden	Deposition	Upper crust (continental, granite)_Facies_Map	1	10
100	Base_Underburden	Horizon_100					

Name	Lithology Value	TOC Mode	TOC Value (%)	Kinetics	HI Mode	HI Value (mgHC/gTOC)	Petroleum System Elements
Overburden	Lundsnee_Overburden_Permeable						Overburden Rock
Test	Lundsnee_reservoir_test						Reservoir Rock
Upper crust (continental, granite)_Facies	Lundsnee_Basement_permeable						Underburden Rock

Experiment 3a:

Age (Ma)	Horizon	Depth Map	Layer	Event Type	Facies Map	No. of Sublayers	Max. Time Step (Ma)
0	Top_8	Horizon_0		8 Deposition	Overburden_Map	1	10
10	Top_7	Horizon_10		7 Deposition	Overburden_Map	1	10
20	Top_6	Horizon_20		6 Deposition	Overburden_Map	1	10
30	Top_5	Horizon_30		5 Deposition	Overburden_Map	1	10
40	Top_4	Horizon_40		4 Deposition	Overburden_Map	1	10
50	Top_3	Horizon_50		3 Deposition	Overburden_Map	1	10
60	Top_2	Horizon_60		2 Deposition	Overburden_Map	1	10
70	Top_1	Horizon_70		1 Deposition	Overburden_Map	1	10
80	Top_Test	Horizon_80	Test	Deposition	Test_Map	1	10
90	Top_Underburden	Horizon_90	Underburden	Deposition	Upper crust (continental, granite)_Facies_Map	1	10
100	Base_Underburden	Horizon_100					

Name	Lithology Value	TOC Mode	TOC Value (%)	Kinetics	HI Mode	HI Value (mgHC/gTOC)	Petroleum System Elements
Overburden	Lundsnee_Overburden_Sealing						Overburden Rock
Test	Shale (organic rich, 20% TOC)	Value		20 Behar_et_al(1997)_TII(PB)	Value		500 Source Rock
Upper crust (continental, granite)_Facies	Lundsnee_Basement_sealing						Underburden Rock

Experiment 3b:

Age (Ma)	Horizon	Depth Map	Layer	Event Type	Facies Map	No. of Sublayers	Max. Time Step (Ma)
0	Top_8	Horizon_0		8 Deposition	Overburden_Map	1	10
10	Top_7	Horizon_10		7 Deposition	Overburden_Map	1	10
20	Top_6	Horizon_20		6 Deposition	Overburden_Map	1	10
30	Top_5	Horizon_30		5 Deposition	Overburden_Map	1	10
40	Top_4	Horizon_40		4 Deposition	Overburden_Map	1	10
50	Top_3	Horizon_50		3 Deposition	Overburden_Map	1	10
60	Top_2	Horizon_60		2 Deposition	Overburden_Map	1	10
70	Top_1	Horizon_70		1 Deposition	Overburden_Map	1	10
80	Top_Test	Horizon_80	Test	Deposition	Test_Map	1	10
90	Top_Underburden	Horizon_90	Underburden	Deposition	Upper crust (continental, granite)_Facies_Map	1	10
100	Base_Underburden	Horizon_100					

Name	Lithology Value	TOC Mode	TOC Value (%)	Kinetics	HI Mode	HI Value (mgHC/gTOC)	Petroleum System Elements
Overburden	Lundsnee_Overburden_Permeable						Overburden Rock
Test	Shale (organic rich, 20% TOC)	Value		20 Behar_et_al(1997)_TII(PB)	Value		500 Source Rock
Upper crust (continental, granite)_Facies	Lundsnee_Basement_permeable						Underburden Rock

Experiment 4a:

Age (Ma)	Horizon	Depth Map	Layer	Event Type	Facies Map	No. of Sublayers	Max. Time Step (Ma)
0	Top_8	Horizon_0		8 Deposition	Overburden_Map	1	10
10	Top_7	Horizon_10		7 Deposition	Overburden_Map	1	10
20	Top_6	Horizon_20		6 Deposition	Overburden_Map	1	10
30	Top_5	Horizon_30		5 Deposition	Overburden_Map	1	10

40 Top_4	Horizon_40	4 Deposition	Overburden_Map	1	10
50 Top_3	Horizon_50	3 Deposition	Overburden_Map	1	10
60 Top_2	Horizon_60	2 Deposition	Overburden_Map	1	10
70 Top_1	Horizon_70	1 Deposition	Overburden_Map	1	10
80 Top_Test	Horizon_80	Test Deposition	Test_Map	1	10
90 Top_Underburden	Horizon_90	Underburden Deposition	Upper crust (continental, granite)_Facies_Map	1	10
100 Base_Underburden	Horizon_100				

Name	Lithology Value	TOC Mode	TOC Value (%)	Kinetics	HI Mode	HI Value (mgHC/gTOC)	Petroleum System Elements
Overburden	Lundsnee_Overburden_Sealing						Overburden Rock
Test	Shale (organic rich, 20% TOC)	Value		20 Behar_et_al(1997)_TII(PB)	Value		500 Source Rock
Upper crust (continental, granite)_Facies	Lundsnee_Basement_sealing						Underburden Rock

Experiment 4b:

Age (Ma)	Horizon	Depth Map	Layer	Event Type	Facies Map	No. of Sublayers	Max. Time Step (Ma)
0 Top_8	Horizon_0			8 Deposition	Overburden_Map	1	10
10 Top_7	Horizon_10			7 Deposition	Overburden_Map	1	10
20 Top_6	Horizon_20			6 Deposition	Overburden_Map	1	10
30 Top_5	Horizon_30			5 Deposition	Overburden_Map	1	10
40 Top_4	Horizon_40			4 Deposition	Overburden_Map	1	10
50 Top_3	Horizon_50			3 Deposition	Overburden_Map	1	10
60 Top_2	Horizon_60			2 Deposition	Overburden_Map	1	10
70 Top_1	Horizon_70			1 Deposition	Overburden_Map	1	10
80 Top_Test	Horizon_80	Test		Test Deposition	Test_Map	1	10
90 Top_Underburden	Horizon_90	Underburden		Underburden Deposition	Upper crust (continental, granite)_Facies_Map	1	10
100 Base_Underburden	Horizon_100						

Name	Lithology Value	TOC Mode	TOC Value (%)	Kinetics	HI Mode	HI Value (mgHC/gTOC)	Petroleum System Elements
Overburden	Lundsnee_Overburden_Permeable						Overburden Rock
Test	Shale (organic rich, 20% TOC)	Value		20 Behar_et_al(1997)_TII(PB)	Value		500 Source Rock
Upper crust (continental, granite)_Facies	Lundsnee_Basement_permeable						Underburden Rock